Volume 2 | Number 29 | 7 August 2014 | Pages 10977–11524

Journal of Materials Chemistry A

Materials for energy and sustainability

www.rsc.org/MaterialsA

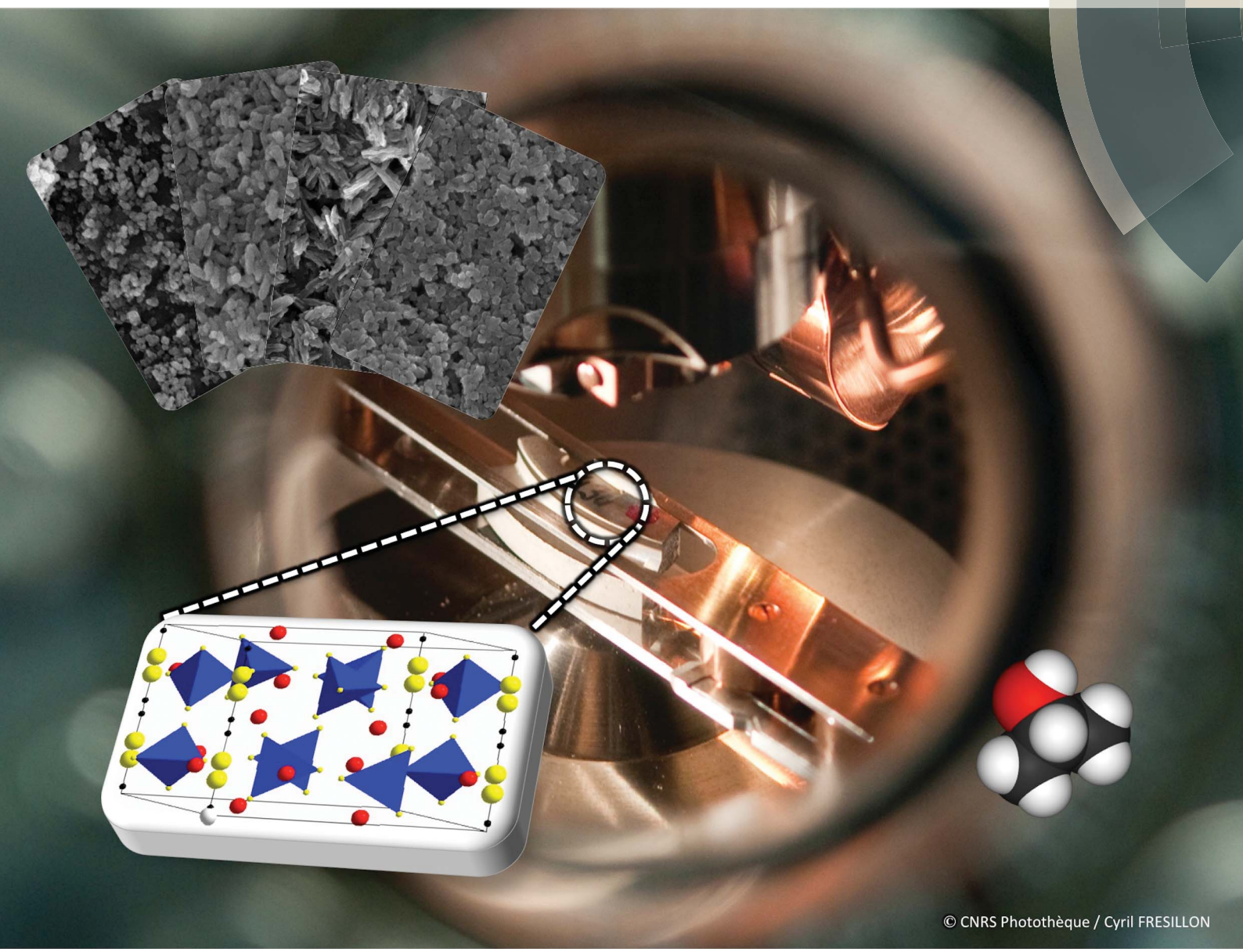

ISSN 2050-7488

ROYAL SOCIETY OF CHEMISTRY

PAPER

Franck Dumeignil *et al.*

Structural, textural and acid–base properties of carbonate-containing hydroxyapatites

Journal of Materials Chemistry A

PAPER

View Article Online
View Journal | View Issue

Cite this: J. Mater. Chem. A, 2014, 2, 11073

Structural, textural and acid–base properties of carbonate-containing hydroxyapatites†

Lishil Silvester,[ab] Jean-François Lamonier,[ab] Rose-Noëlle Vannier,[abc] Carole Lamonier,[ab] Mickaël Capron,[ab] Anne-Sophie Mamede,[abc] Frédérique Pourpoint,[abc] Antonella Gervasini[d] and Franck Dumeignil*[abe]

Received 3rd April 2014
Accepted 6th May 2014

DOI: 10.1039/c4ta01628a

www.rsc.org/MaterialsA

Carbonate-containing hydroxyapatites with different Ca/P ratios and optionally containing Na^+ cations were successfully synthesized using a precipitation method. The solids were extensively characterized by XRD, LEIS, XPS, IR, TGA and NMR. Further, their acid–base properties were determined by NH_3-TPD, PEA-XPS, CO_2-TPD and by pulsed liquid chromatography using benzoic acid as a probe. The so-obtained structural, textural and acid–base properties could be finely correlated to give a clear picture of the system. The acidic properties of hydroxyapatites were attributed to Ca^{2+}, surface HPO_4^{2-} and OH^- vacancies and the basic properties were attributed to PO_4^{3-}, OH^- and CaO species. The fine-tuning of the amount, of the nature and the strength of acid–base properties derived by varying the carbonate content in hydroxyapatites can find applications in catalysis, which was illustrated by isopropanol reactivity.

1 Introduction

Natural hydroxyapatite (HAP), with the formula $Ca_{10}(PO_4)_6(OH)_2$, is the most stable calcium phosphate salt, and is the main inorganic constituent of biological hard tissues in animal organisms. It can be synthesized at various temperatures, typically below 373 K, and at a pH between 4 and 12. It drives a considerable interest in medical applications, in chromatography, as a fertilizer, in the pharmaceutical industry, and in the field of catalysis.[1–3] HAP contains both acidic and basic sites in a single crystal lattice,[4,5] and can thus be applied to reactions requiring bifunctional solid catalysts containing both antagonist functionalities, such as the Guerbet reaction,[6] the Michael addition, the Knoevenagel condensation,[7] the Claisen–Schmidt condensation or the Friedel-Crafts reaction.[8] The aforementioned native HAP allows large variations in compositions, and, as a general matter, the so-called 'HAPs' are highly non-stoichiometric solids with the general formula '$Ca_{10-x}(PO_4)_{6-x}(HPO_4)_x(OH)_{2-x}$', with $0 < x \leq 1$. This yields a family of compounds with very different properties, from more acidic solids in the case of deficient HAPs ($x > 0$) to solids more and more basic when approaching the stoichiometry of the native HAP ($x = 0$), this latter being, therefore, predominantly basic.[2,9,10] The Ca/P ratio is commonly used as an index of their non-stoichiometry (the stoichiometric ratio being 1.67) and of their acid–base behaviour. It is well known that HAPs act as solid acid catalysts when Ca/P $\approx$ 1.50, and develop both the acidic and the basic characteristics when the Ca/P ratio is between 1.50 and 1.67.[11–15] In addition to varying the Ca/P ratio, the surface acid–base properties of the HAPs can also be tuned by replacing Ca^{2+} ions by vacancies or cations such as Sr^{2+}, Mg^{2+}, Na^+, K^+, *etc.* Substitution of OH^- anions by vacancies, F^-, Cl^-, CO_3^{2-} and/or PO_4^{3-} anions by CO_3^{2-}, HPO_4^{2-}, VO_4^{3-}, *etc.*, are other possibilities. The structure of HAP comprises three-dimensional networks of hexagonally packed tetrahedral PO_4^{3-} ions. These ions make a first channel around Ca^{2+} ions [Ca(I)] with a diameter of 2.5 Å.[16,17] A second channel with a diameter of 3.5 Å, bordered by triangular Ca^{2+} ions [Ca(II)], hosts the OH^- species along the *c*-axis.[18] The structure is flexible to both cationic and anionic substitutions, which yields the aforementioned possibility of modulating the number of acid–base sites in the HAP crystal. Cations can substitute either Ca(I) or Ca(II) ions or both ions simultaneously, and anions can replace either OH^- or PO_4^{3-} ions or both.[11] The general formula for carboapatites, in which CO_3^{2-} ions can be located in two different positions, is $Ca_{10}[(PO_4)_{6-x-y}(HPO_4)_x(CO_3)_y][(OH)_{2-(x+y)}(CO_3)_{x+y}]$, considering that the charge loss due to the PO_4^{3-} substitution (B-type substitution) is counterbalanced by addition of CO_3^{2-} in the OH^- sites (A-sites).[19] If some defects arise due to the formation

[a]Université Lille Nord de France, 59000 Lille, France. E-mail: franck.dumeignil@univ-lille1.fr; Fax: +33(0)3 20 43 65 61; Tel: +33(0)3 20 43 45 38

[b]CNRS UMR 8181, Unité de Catalyse et Chimie du Solide, Cité scientifique, Bâtiment C3, 59655 Villeneuve d'Ascq, France

[c]ENSCL, Villeneuve d'Ascq, F-59655, France

[d]Dipartimento di Chimica, Universita degli Studi di Milano, Via Golgi 19, 20133 Milan, Italy

[e]Institut Universitaire de France, Maison des Universités, 103 Boulevard Saint-Michel, 75005 Paris, France

† Electronic supplementary information (ESI) available: Examples of XRD diffractogram refinement; temperature-programmed XRD patterns; derived ATG profiles; 11P CP MAS-NMR spectra. See DOI: 10.1039/c4ta01628a

of vacancies or related substitution of Ca by Na, charge will be compensated by less carbonates in A-sites.

Different substitutions not only result in a variation in the balance between the acidic and the basic nature of the solid HAPs surface, but may also change their morphology. Some studies have reported a correlation between the exposure to the surface of HAP specific components such as Ca^{2+} and PO_4^{3-} groups, and the type of crystallite growth.[3,19–21] However, their conclusions are contradictory and a deeper understanding is then required. In the present work, using X-ray diffraction (XRD) & Rietveld refinement as well as TGA, we precisely determined the crystallite nature and the global formula of HAPs prepared by varying the Ca/P ratio (or the carbonate content). The types of carbonate substitution were determined by IR spectroscopy. The presence of orthophosphate and of HPO_4^{2-} groups in the HAPs was qualitatively evaluated with the help of CP MAS-NMR and 2D-HETCOR NMR spectroscopy. Further, X-ray Photoelectron Spectroscopy (XPS) complemented by Low Energy Ion Scattering (LEIS) was used to precisely determine the surface composition of the solids, in order to enable identification of any potential correlation with the crystallite growth/morphology. The total number of acidic and of basic sites in the HAPs was determined by Thermo-Programmed Desorption of NH_3 (TPD-NH_3) and of CO_2 (TPD-CO_2), respectively. We also determined the distribution of the nature of the surface acid sites (Lewis & Brønsted) by XPS after adsorption of 2-phenylethylamine (PEA) used as a probe molecule.[22] The pulse liquid chromatographic technique[23] using benzoic acid as a probe molecule was further used to determine the amount and strength of basic sites in the hydroxyapatites directly in the liquid phase. The surface acid–base reactivity was further evaluated using isopropanol reactivity as a test model reaction.

2 Experimental

2.1 Materials

Reagent grade chemicals such as calcium nitrate tetrahydrate, $Ca(NO_3)_2\cdot 4H_2O$ (≥99.0%); ammonium dihydrogen phosphate, $(NH_4)H_2PO_4$ (≥98.0%); sodium nitrate, $NaNO_3$ (99.0%); and sodium carbonate, Na_2CO_3 (≥99.0%) (Sigma Aldrich) were used as starting materials.

2.2 Sample preparation

All the solids were synthesized by using a precipitation method reported elsewhere.[24] Deficient and stoichiometric HAPs were prepared by fixing the Ca/P molar ratios of the synthesis solutions at 0.9 and 1.67, respectively. Two carbonated apatites with and without sodium were synthesized by moderately increasing the (Ca + Na)/P ratio of the solutions from the stoichiometric value of 1.67 to 2, with a Ca/Na molar ratio of 5.7 for the Na-containing solid. Finally, two carbonate-rich apatites with and without sodium were synthesized by increasing the (Ca + Na)/P ratio of the solutions from the stoichiometric value of 1.67 to 5.5 with a Ca/Na molar ratio of 5 for the Na-containing solid. The detailed preparation procedures of these samples are given below.

A stoichiometric hydroxyapatite (Hap) was synthesized by adding dropwise 300 mL of an aqueous solution containing 0.167 mol of $Ca(NO_3)_2\cdot 4H_2O$ to 1000 mL of a 0.1 mol of $(NH_4)H_2PO_4$ solution placed under stirring at 353 K. The pH during synthesis was maintained at 10 by properly adding a 25% NH_4OH solution. The formed precipitate was slowly filtered, washed with hot water, and dried at 353 K before being calcined for 4 h under oxygen at 673 K (2 K min^{-1}). Lowering the calcium quantity in the solution from 0.167 mol to 0.09 mol resulted in the formation of a calcium deficient hydroxyapatite (HapD).

For carbonated hydroxyapatite with Ca/P > 1.67, CO_2 was naturally introduced from the atmosphere as CO_3^{2-} anions, which were incorporated to compensate the charge due to excess calcium cations in the apatite solids. In this respect, the carbonated apatite (Hap-CO_3) was prepared by using a Ca/P molar ratio of 2 in the precursor solutions instead of the stoichiometric value of 1.67. The same procedure was used to synthesize a sodium-containing carbonate apatite (HapNa-CO_3) prepared with a Ca/Na molar ratio of 5.7, keeping a (Ca + Na)/P molar ratio of 2.

A carbonate-rich hydroxyapatite was synthesized by adding dropwise an aqueous solution of 0.1 mol of $(NH_4)H_2PO_4$ (0.1 M) to a 300 mL solution containing 0.55 mol of calcium nitrate placed under stirring at 353 K. The higher Ca/P molar ratio of 5.5 compared to the stoichiometric value of 1.67 allowed us to introduce a higher quantity of carbonate ions in the synthesized hydroxyapatite. The corresponding solid was denoted as HapE-CO_3, which is thus a sodium-free carbonate-rich apatite. Also more carbonate ions and sodium ions were introduced in a last sample, using sodium carbonate (5.83 g) dissolved in 1000 mL of an ammonium hydrogen phosphate solution (0.1 M). The Ca/Na molar ratio of the solution was fixed at 5. In that case, the resulting solid was a sodium-containing carbonate-rich apatite denoted as HapE-Na-CO_3.

2.3 Characterization methods

The chemical composition of the samples was determined at the 'Service Central d'Analyses du CNRS' (Vernaison, France) using Inductively Coupled Plasma Mass Spectrometry ICP-MS. Before ICP-MS chemical analyses, the samples were dissolved in acidic media.

The specific surface areas were determined using a conventional multipoint BET nitrogen adsorption method with a Micrometrics Tristar II apparatus. Prior to nitrogen adsorption, the samples were outgassed for 4 h at 423 K under nitrogen flow.

Thermo gravimetric analysis (TGA) was performed using a Thermal Analysis instrument (TG92 Setaram) connected to a mass spectrometer (Omnistar), on 15 mg of sample. The weight loss was recorded under synthetic air, at a heating rate of 10 K min^{-1} from room temperature to 1273 K.

Routine powder X-ray diffractograms were recorded at room temperature (RT) using a Bruker AXS D8 Advance diffractometer working in a Bragg-Brentano geometry and equipped with a

LynxEye Super Speed detector. Data were collected using the CuK$\alpha_{1,2}$ line in the 10–90° 2θ range with a 0.02° 2θ step. The Fullprof Suite program was used for Rietveld refinement.[25] The Thompson-Cox-Hastings pseudo-Voigt function was chosen for describing the peak profiles. LaB_6 was used as a standard to derive the instrument resolution.[26] Here, an anisotropic size-broadening model based on linear combination of spherical harmonics was used to simulate the size broadening, and 6 additional parameters were refined. From this refinement, the individual size was derived for each crystallographic plane.

Temperature-programmed XRD was also carried out on a Bruker AXS D8 advanced apparatus equipped with an Anton Paar HTK1200N high temperature chamber, and connected to a VANTEC fast linear detector, which enables short acquisition time. Each sample was deposited on a Pt sheet. The experiments were performed by increasing the temperature from 323 K to 1273 K, while acquiring a diffractogram at every 25 K. The data acquisition parameters correspond to an angular range of 10°–70° with a step of 0.015° and an acquisition time of 0.22 s per step.

The morphology of the catalysts was observed using Scanning Electron Microscopy images recorded on a Hitachi S-4700 apparatus with a 50k magnification.

Transmission infrared (IR) spectra were recorded from 400 cm^{-1} to 4000 cm^{-1} at room temperature under vacuum in a Nicolet 460 Fourier transform infrared spectrometer. The samples were prepared by intimately mixing 1 mg of powdered sample with 150 mg of dried KBr.

All the 1D and 2D MAS-NMR (CP HETCOR) spectra were recorded at room temperature using a Bruker Advance spectrometer working at a ^1H Larmor frequency of 400 MHz (9.4 T). The resonance frequency of ^{31}P was then 161.9 MHz. A Bruker 4 mm CP MAS probe was used to perform all the experiments at a spinning speed of 10 kHz. The chemical shifts were determined using tetramethylsilane (TMS) (0 ppm) and H_3PO_4 ($\delta = 0$ ppm) as reference compounds, for ^1H and ^{31}P spectra, respectively.

The surface Ca/P ratio and the CO_3^{2-} content of the HAPs were determined from the areas of the Ca 2p, P 2p and C 1s photopeaks recorded using XPS on a Kratos Axis Ultra^{DLD} spectrometer. Photoelectrons generated by a monochromatic Al-Kα X-ray radiation source operating at 150 W (15 kV, 10 mA) having initial kinetic energies of up to 1486.7 eV ensured an average depth for an electron escape of ~1–10 nm. High-resolution scans were acquired with 40 eV pass energy and 300 ms dwell times. All the resulting binding energy values were corrected using the C 1s peak (C–C) fixed at 285 eV as a reference.

LEIS spectra were recorded using a Qtac^{100} spectrometer (ION TOF Gmbh). The spectra were recorded using a 3 keV $^4He^+$ beam. Assuming a sputter yield of 0.1 atoms per He-ion under a 4 nA target current, the total dose density was less than 3.0×10^{13} atoms per cm^2.

The density of acid sites in the samples was determined by TPD-NH_3 using a Micrometrics apparatus equipped with a mass spectrometer. 150 mg of sample were purged for 30 min in a He flow of 40 mL min^{-1} at 673 K before being naturally cooled to room temperature. The sample was then contacted with a 10% NH_3/He atmosphere during 30 min in a 30 mL min^{-1} flow before being further purged for 2 h at room temperature under 50 mL min^{-1} He flow. After purging, the temperature was raised at a rate of 10 K min^{-1} to 873 K in under 30 mL min^{-1} He flow. The quantity of desorbed NH_3 was determined by mass spectrometry using the peak with $m/z = 15$.

The density in basic sites was similarly evaluated using TPD-CO_2 with 5% CO_2/He on the same micrometrics apparatus under the same conditions as those employed for TPD-NH_3. The quantity of basic sites was determined by mass spectrometry using the peak with $m/z = 44$.

The nature of the medium–strong acid sites was then determined by PEA-XPS analysis, using the adsorption of PEA as a probe molecule before XPS measurement.[22] Prior to the adsorption, the calcined samples were outgassed at 523 K for 4 h under Ar flow. The cleaned powder was then transferred to a glass cell connected with vacuum/gas lines, and liquid PEA (purity >99%, purchased from Fluka) was introduced in the cell to cover up the powder during 2 h under Ar flow. Then, the excess of non-adsorbed PEA was removed by filtration using primary vacuum under Ar flow. The sample was then directly transferred to the chamber of the spectrometer for analysis. PEA is a strong base that can be retained by weak, medium, and strong acid sites over solid surfaces. Note that XPS measurements of PEA provide information only on the strong and medium acid sites and not on the weakest sites, which cannot hold this probe under the ultra-high vacuum conditions of the analyses, the latter being desorbed under such harsh conditions.[22]

A pulsed liquid chromatographic technique[23] was further used for the determination, directly in a liquid phase, of the amount of the surface basic sites using benzoic acid adsorption. All the experiments were conducted using a liquid chromatograph (HPLC) connected to a Waters model 510 pump, a Rheodyne 7725 injector and a Waters model 2487 UV detector coupled to a personal computer for the collection and data processing. The sample was placed in a sample holder, in the form of a small stainless steel tube (*i.d.* = 2 mm, length = 12 cm) placed in replacement of the chromatographic column in the HPLC. Prior to analysis, the sample was placed at the centre of the sample holder tube, supported by silica wool and acid-washed sea sand (Fluka), which are totally inert towards the adsorption of the benzoic acid probe. For each experiment, a weighed amount of fresh sample was outgassed in a furnace for 16 h at 623 K under air flow (8 mL min^{-1}), and then the cell was evacuated under vacuum before being filled with cyclohexane as an apolar-aprotic solvent. The linearity of the chromatographic response as a function of the benzoic acid concentration in cyclohexane was checked by injecting known concentrations of benzoic acid solutions. In each adsorption test, pulses consisting of 20 μl benzoic acid solution of a known concentration of 0.05 mol L^{-1} were passed through the sample at a constant cyclohexane flow rate (0.5 mL min^{-1}). The unabsorbed amount of benzoic acid after each pulse was recorded until the sample saturation (total recovery of the benzoic acid in the injected pulse and completion of the first cycle). If a 1 : 1 adsorption stoichiometry is assumed in this cycle, the total number of basic sites corresponds to the total amount of benzoic acid adsorbed

on the sample. In the second cycle, the sample was purged with cyclohexane (0.05 mol L^{-1}) to remove the weakly adsorbed benzoic acid molecules on the solid surface. Finally, a third benzoic acid adsorption cycle similar to the first cycle was performed which determines the amount of benzoic acid molecules removed during the purge and therefore the weak basic sites. The amount of strong basic sites is thus calculated by the difference between the total amount of basic sites (titrated in the first cycle) and the amount of weak basic sites obtained in the third cycle.

Acid–base properties of all the solids were finally evaluated using a test catalytic reaction, namely the isopropanol conversion, which gives propylene (and also small amounts of di-isopropylether, which was detected over some samples), over acid sites and acetone over basic sites. The selectivity of the samples was compared at 20% iso-conversion of isopropanol, which was adjusted by properly setting the reaction temperature (typically between 548 K and 623 K). The reaction was carried out in a glass flow reactor working at atmospheric pressure. The solid was ground and sieved to particle size in the 80–100 μm range. This powdered and sieved material (100 mg) was then mixed with an equal quantity of carborundum (120 μm) and used as a catalyst bed followed by another layer of 500 mg carborundum to ensure thermal homogeneity and smooth heat transfer inside the reactor. The reactant feed containing 2 mol% of isopropanol was obtained by bubbling He (25 mL min^{-1}) through liquid isopropanol placed in a saturator maintained at 283 K. The reaction products were analysed on-line using a gas chromatograph equipped with a HP-INNOWax column (l = 30 m, i.d. = 0.25 mm, film thickness = 0.50 μm) and a flame ionization detector.

3 Results and discussion

3.1 Bulk composition of the solids

It is known that the Ca/P atomic ratios obtained by chemical analysis of the final solids differ from those of the solutions used during their synthesis.[27,28] The Ca/P atomic ratios of all the prepared samples (Table 1) were indeed lower than the Ca/P molar ratios in the preparation solutions, except for the deficient and the stoichiometric apatites, namely HapD and Hap. Indeed, for HapD and Hap, the Ca/P atomic ratios in the solid were 1.62 and 1.69, respectively, compared with 0.9 and 1.67 fixed during their synthesis. The chemical compositions of the solids further show that an increase in the Ca/P ratio was accompanied by a linear increase in the carbon content (Fig. 1), which can most probably be attributed to the introduction of carbon in the form of carbonate ions in the apatite structure, in substitution to phosphate ions (*vide supra*).

3.2 Specific surface areas

The specific surface areas of all the calcined solids were larger than 100 $m^2 g^{-1}$, except for the carbonate-rich apatites, namely HapE-CO_3 and HapE-Na-CO_3, with 76 and 72 $m^2 g^{-1}$, respectively (Table 1). Hence, this underlines that this preparation method carried out in an open atmosphere can provide apatites with high surface areas, which however decreased a little bit when introducing CO_3^{2-} ions in the case of carbonate-rich solids.

3.3 Structure of the solids

3.3.1 Crystallographic structure. All the X-ray diffraction patterns suggested the exclusive presence of the crystalline hydroxyapatite phase (JCPDS 01-084-1998) with small differences in Bragg peak positions (Fig. 2).[29] A small shift of the (3 0 0) Bragg peak towards higher 2θ values associated with better crystallinity was observed when the carbonate content increased from HapD ($2\theta = 32.8°$) to HapE-Na-CO_3 ($2\theta = 33.4°$).

The apatite structure was refined in the $p6_3/m$ space group, using the structure model proposed by Hughes *et al.*[29] The

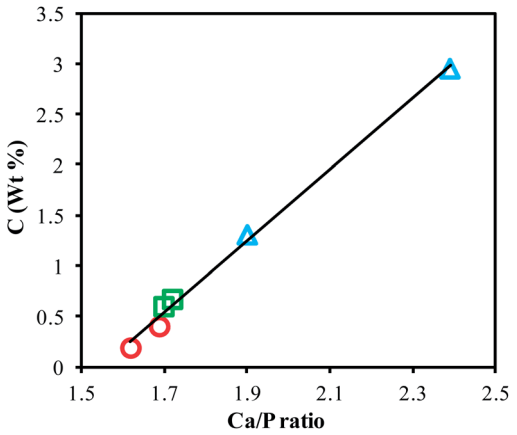

Fig. 1 Carbon content as a function of the bulk Ca/P ratio of the solids (circles represent HapD and Hap, squares for carbonated apatites, namely Hap-CO_3 and HapNa-CO_3, and triangles for carbonate-rich apatites, namely HapE-CO_3 and HapE-Na-CO_3).

Table 1 Chemical composition and specific surface area of the prepared solids calcined at 673 K

Type of solid	Name	(Ca + Na)/P molar ratio in solutions	Ca/P atomic ratio (ICP)	Ca (wt%)	P (wt%)	Na (wt%)	C (wt%)	Specific surface area ($m^2 g^{-1}$)
Deficient	HapD	0.9	1.62	37.06	17.69	—	0.18	124
Stoichiometric	Hap	1.67	1.69	38.45	17.54	—	0.40	114
Carbonated	Hap-CO_3	2.0	1.70	38.10	17.29	—	0.59	107
Carbonated	HapNa-CO_3	2.0	1.72	38.17	17.14	0.64	0.67	109
Carbonate-rich	HapE-CO_3	5.5	1.90	37.03	15.04	—	1.30	76
Carbonate-rich	HapE-Na-CO_3	6.6	2.39	39.47	12.75	<0.3	2.95	72

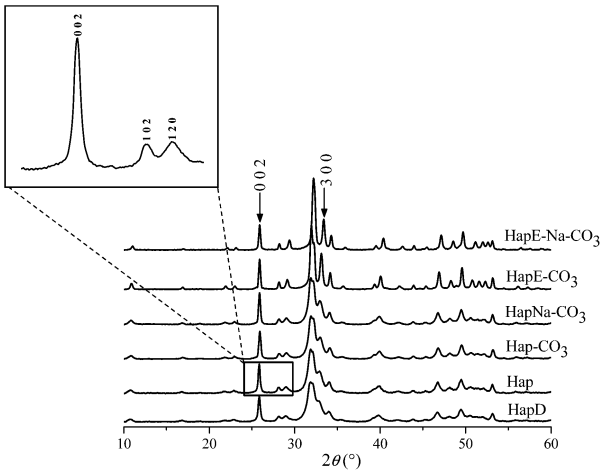

Fig. 2 XRD patterns of the calcined solids.

atomic positions of all the atoms were refined. To take into account the thermal vibrations, an overall parameter was used for all the crystallographic sites. For all the samples, the XRD pattern showed a thinner Full Width at Half Maximum (FWHM) for the (0 0 2) reflection compared to the FWHM of the other reflections (see the inset in Fig. 2 and S1†), indicating the presence of anisotropic crystallites. Therefore, an anisotropic size-broadening model based on linear combination of spherical harmonics was used to simulate the size broadening,[30] taking into account the instrument resolution from a LaB_6 pattern. From this model, the crystallite shape was deduced. For Hap and HapE-Na-CO_3 taken as examples, a good agreement was obtained between the calculated and the experimental data in all the solids (Fig. S2†). All the results are summarized in Table 2.

As expected, a decrease in the *a* values with increasing the carbonate content from 9.4210(4) Å in HapD to 9.3111(8) Å in HapE-Na-CO_3 was observed except for Hap, which showed a lower *a* value compared to Hap-CO_3. This observation is in good agreement with the partial substitution of phosphate groups by carbonate ions, as previously reported.[32–34] In contrast, an increase in the carbonate content led almost to no evolution of the *c* value, which corresponds to the stacking direction of the apatite structure. Only a slight increase in the *c* value was observed for the sodium-containing samples (HapNa-CO_3 & HapE-Na-CO_3), as already reported for sodium-substituted apatites compared to pure Hap.[33,35]

While structure models have been proposed for carbonate-containing apatites,[33] because of the too low X-ray scattering length of carbon atoms, it was not possible here to refine the carbonate positions. However, we could confirm the partial substitution of phosphate groups by refining the occupancy of phosphorous sites, thereby indirectly determining the occupancy of carbonates from the vacancies in the phosphorous sites. The phosphorous vacancies were then refined for all the compositions (Table 2). As expected, the refinements led to the lowest phosphorous occupancies of 89.4(4)% and 78.6(4)%, respectively in the carbonate-rich HapE-CO_3 and HapE-Na-CO_3 samples, compared to the other apatites. This reveals the presence of higher amounts of carbonates in the phosphorous sites of carbonate-rich apatites, which is in good agreement with the introduction of carbonates in the P sites (B-type apatite sites). It was not possible to refine the Na occupancy in the calcium site of HapE-Na-CO_3, in good agreement with the low sodium amount observed by ICP. In the case of HapNa-CO_3, introduction of sodium in the Ca(I) site led to a small occupancy corresponding to 0.18(9) Na for 9.82 calcium atoms in the apatite, in rather good agreement with the sodium amount measured by ICP (0.28 wt%). Moreover, introduction of Na in the Ca(II) sites led to a negative occupancy, indicating a preference of Na for the Ca(I) sites, and, therefore, in the refinement, sodium was introduced only in the Ca(I) sites. For the deficient apatite (HapD), refinement of calcium sites occupancies led to unrealistic values, which were higher than '1'. Therefore, the calcium occupancy was fixed to 1, and it was thus not possible to confirm the calcium deficiency only using X-ray diffraction. Moreover, for this composition, a phosphorous occupancy of 97.0(4)% was obtained, suggesting the presence of a small amount of carbonates in the B sites.

Table 2 Cell parameters, phosphorus occupancy and crystallite size determined using Rietveld refinement

Solids	Cell parameters		Phosphorus site occupancy (%)	(Ca + Na)/P [ICP]	Crystallite size (nm) corresponding to the crystallographic plane		Length/thickness ratio
	a (Å)	*c* (Å)			(1 0 0)	(0 0 1)	(0 0 1)/(1 0 0)
HapD	9.4210(6)	6.8853(4)	97.0(4)	1.72(5) [1.62]	7	22	3.2
Hap	9.4103(5)	6.8871(4)	94.6(4)	1.76(2) [1.69]	8	26	3.2
Hap-CO_3	9.4142(5)	6.8876(4)	93.8(4)	1.77(2) [1.70]	9	30	3.3
HapNa-CO_3[a]	9.4106(6)	6.8909(4)	93.8(4)	1.78(2) [1.77]	10	36	3.6
HapE-CO_3	9.3742(5)	6.8891(4)	89.4(4)	1.87(2) [1.90]	23	55	2.4
HapE-Na-CO_3	9.3111(8)	6.8982(6)	78.6(4)	2.12(2) [2.39]	23	41	1.8

[a] Na occupancy was refined in the case of HapNa-CO_3 (see text). N.B. standard deviation for unit cell parameters, phosphorous occupancy and (Ca + Na)/P ratio are given in brackets by taking into account the Berar factor.[31]

Fig. S3† shows that the (Ca + Na)/P ratio refined from XRD data increased linearly with the same ratio determined by ICP. However, the XRD-deduced ratios exhibited a slight deviation from the so-to-speak ideal ICP ratio, especially for HapE-Na-CO_3 with a higher Ca+Na/P ratio compared to the other apatites. In terms of the phosphorous site occupancy, this makes a difference of 10% with 79% (ICP) to be compared to 69% (XRD). This deviation can be explained by the limited accuracy on the phosphorus occupancy from XRD data, since the overall parameter was used in refinement for all the crystallographic sites, and the thermal vibrations and occupancies in such refinement are strongly correlated.

3.3.2 Crystallite and grain shape. As aforementioned, an anisotropic size-broadening model was used to deduce the crystallite size. As shown in Table 2, the crystallite size along the (1 0 0) and (0 0 1) planes, determined by Rietveld refinement, indicated that the crystal growth increased with an increase in the Ca/P ratio or carbonate content (Table 2), these parameters being correlated. The crystallite size was much higher for carbonate-rich HapE-CO_3 (23 nm & 55 nm) and HapE-Na-CO_3 (23 nm & 41 nm) when compared to stoichiometric Hap (8 nm & 26 nm) (Table 2). The length/thickness ratios of Hap and HapD were identical (3.2), and slightly higher for Hap-CO_3 (3.3) and HapNa-CO_3 (3.6), which contains just a few carbonates, suggesting similar elongated crystallite shapes. In contrast, a lower length/thickness ratio was observed for the apatites rich in carbonates (2.4 & 1.8), thus indicating that the crystallites became more spherical for carbonate-rich apatites (Table 2). To verify whether the crystallite shapes obtained by Rietveld refinement have an influence on the grain shape, scanning electron microscopy pictures were taken. The anisotropy observed by XRD was then confirmed by SEM (Fig. 3). Irregularly shaped agglomerates were observed for stoichiometric (Hap) and deficient apatites (HapD), while flat needle/rod-shaped clusters were observed for the carbonated apatites Hap-CO_3 and HapNa-CO_3. The pictures also revealed capsule and spherically shaped grains for HapE-CO_3 and HapE-Na-CO_3, respectively. In all the cases, the grain shapes were thus in good agreement with the crystallite shape determined by refinement from XRD diffractograms. However, using SEM, bigger particles with length in the order of 100 μm were observed, indicating agglomerated poly-crystallite grains.

3.3.3 Amount and type of carbonate substitution

3.3.3.1 Thermal stability and carbonate content. To check the thermal stability of the apatite solids, temperature-programmed XRD was carried out using 3 selected compositions, namely HapD (a deficient apatite), Hap-CO_3 (carbonated apatite very similar to Hap and HapNa-CO_3), and HapE-Na-CO_3 (a carbonate-rich apatite, similar to HapE-CO_3). The deficient apatite HapD was chosen, since it is supposed to decompose to stoichiometric apatite (Hap-like) and $Ca_3(PO_4)_2$,[27,36] whereas all the other apatites with a Ca/P ratio higher than 1.67 should decompose to stoichiometric apatite and CaO.[27] The so-obtained series of X-ray patterns are shown in Fig. S4.† As expected, HapD decomposed to stoichiometric apatite and $Ca_3(PO_4)_2$ with the appearance of two forms of $Ca_3(PO_4)_2$, namely α-$Ca_3(PO_4)_2$ (JCPDS 01-070-0364) and *syn*-$Ca_3(PO_4)_2$ (JCPDS 00-009-0169), at 973 K. Compared to normal stoichiometric apatites (Ca/P = 1.67), $Ca_3(PO_4)_2$ formed from deficient HapD exhibits a smaller Ca/P ratio of 1.5 and the formation of $Ca_3(PO_4)_2$ is thus an indirect proof of calcium deficiency in HapD. In contrast, for temperatures higher than 998 K, the formation of calcium oxide was observed for Hap-CO_3, and the same transformation was noticed at around 898 K for HapE-Na-CO_3 for which, in addition, a slight modification of the X-ray pattern was noticed at 823 K. It was characterised by a decrease in intensity and an increase in the FWHM of the (0 0 2) Bragg peak and by the appearance of an additional peak around $2\theta = 29.5°$, which further disappeared at 923 K, maybe due to the reconstruction of the apatite structure (Fig. S4†). Since only one additional Bragg peak was observed, it was not possible to go further in the understanding of this modification.

These transformations were further examined by means of thermogravimetric analysis combined with mass spectrometry (Fig. 4), confirming the aforementioned XRD results. For all the compositions, weight losses are due to the release of CO_2 and/or H_2O as observed from the TPD-MS curves (Fig. S5 and S6†). In agreement with previous studies,[24,37] weight losses are attributed to the H_2O and CO_2 desorption from the hydroxyapatite surface below 823 K and to the CO_2 released from the crystal above 923 K. Indeed, in this temperature range, as observed in the TPD-MS curves, the release of H_2O is very low and its corresponding weight loss can be negligible. The thermograms can be divided into three groups, corresponding to the observed shapes of the recorded lines: (a) HapD and Hap-Na-CO_3, (b) Hap and Hap-CO_3 and (c) HapE-CO_3 and HapE-Na-CO_3. In group (a), a clear transition was observed at 973 K in good agreement with the decomposition of HapD observed by X-ray diffraction (Fig. S4(a)†). For the second group (b), the transition occurred at around the same temperature of 973 K, but was not sharp, and a plateau was not obtained at 1273 K. For carbonate-rich apatites HapE-CO_3 and HapE-Na-CO_3 [group (c)], MS curves indicate surprisingly no departure of CO_2 before 873 K. The release of CO_2 in the HAPs started at a lower temperature, and occurred in two steps with a change in the slope around 1000 K, in good agreement with the high temperature X-ray diffraction study. Assuming that the decomposition of all the apatites led to stoichiometric HAP and CaO [except for HapD, for which this is $Ca_3(PO_4)_2$ instead of CaO] at the end of the thermal study, it was possible to calculate the corresponding loss in CO_2 or, otherwise, of CO_3^{2-} moles per apatite formula (Table 3). By comparison with the CO_3^{2-} content in the B sites deduced from Rietveld refinement and the total CO_3^{2-} loss obtained from TGA, the first mass loss was easily attributed to the release of CO_3^{2-} from the A sites (channels) and the second mass loss to the release of CO_3^{2-} from the B sites.

Interestingly, CO_3^{2-} was mainly located in the B sites for HapD, Hap, Hap-CO_3 and HapNa-CO_3 and in both A and B sites for the carbonate-rich apatites, namely, HapE-CO_3 and Hap-E-Na-CO_3. It is worth mentioning that the carbonate content deduced from XRD and TGA was in good agreement with the ICP analysis, confirming the good precision and the reliability/accuracy of the XRD refinement (Table 3). Moreover, a linear increase was observed in the case B-type CO_3^{2-} obtained both

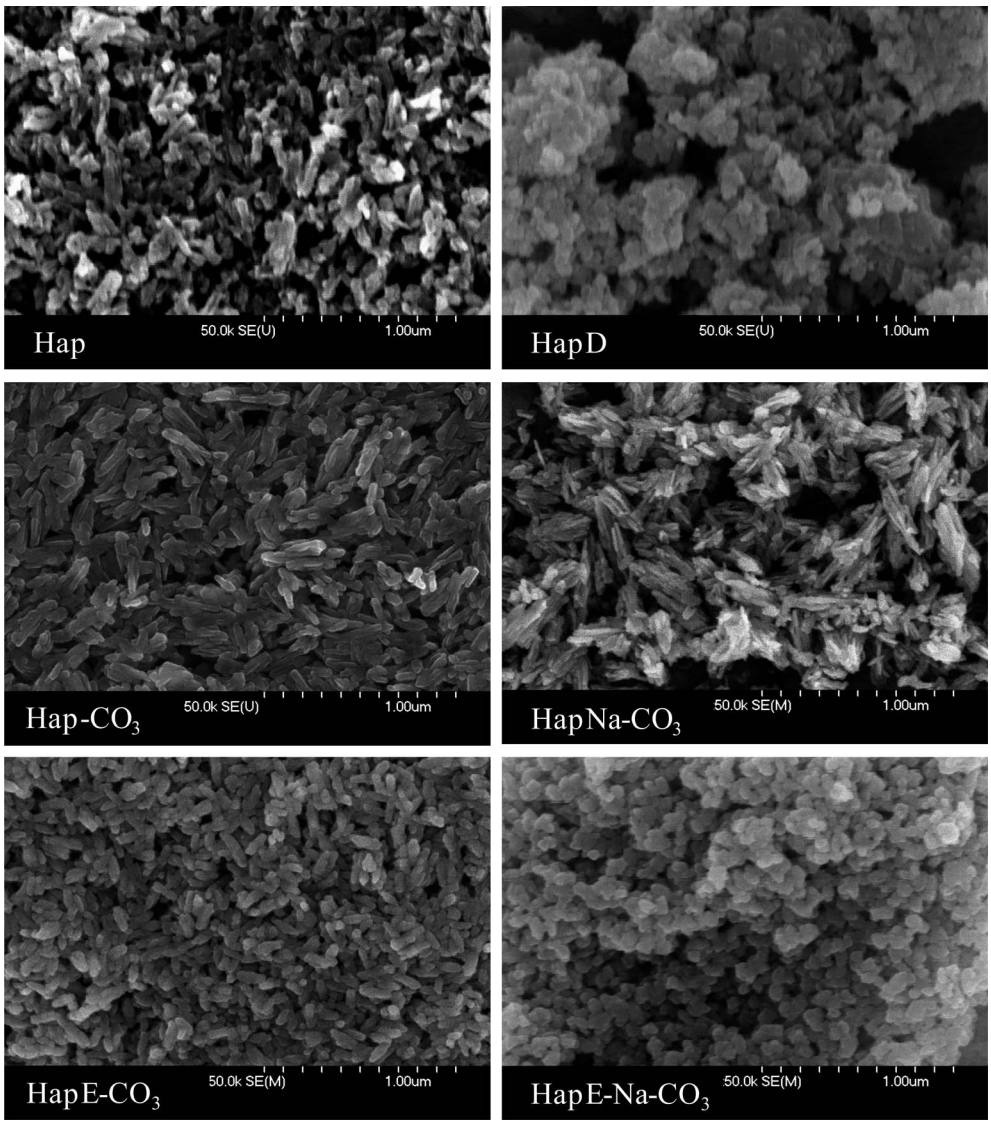

Fig. 3 SEM images of calcined samples at 50.0k magnification.

from TGA and XRD as shown in Fig. 5, in excellent agreement with the theoretical line.

3.3.3.2 A & B-type carbonate substitution. Fig. 6 and 7 represent two domains of the IR spectra of the HAP samples, focused on two different respective spectral regions, namely 700–1800 cm^{-1} and 3300–3700 cm^{-1}. All the IR spectra confirmed the formation of carbonate-containing apatites with bands at 872 cm^{-1}, 1460 cm^{-1} and 1419 cm^{-1}.[38–40]

The fundamental vibrational modes of PO_4 species gave rise to bands at 565 cm^{-1}, 605 cm^{-1}, 963 cm^{-1} and 1030–1100 cm^{-1}, as reported earlier.[41,42] Further, HPO_4^{2-} groups might also be present, with the characteristic band at 872 cm^{-1}. However, this latter is known to overlap with a carbonate band, making straightforward conclusions impossible.[38]

The broad vibrational band in the 3300–3700 cm^{-1} range is due to the presence of adsorbed and constitutive water molecules. The presence of carbonates in B-sites was confirmed by the increase in the intensity of the typical band at 872 cm^{-1} observed in carbonate-rich apatites,[40,43] which could make the presence of HPO_4^{2-} species quite questionable, but these latter were detected using NMR spectroscopy (see Section 3.4). In addition, the peaks at 1460 cm^{-1} and 1419 cm^{-1} can be attributed to CO_3^{2-} substituting PO_4^{3-} groups, which thus lead to the formation of B-type apatites.[39] The band at 3572 cm^{-1} is assigned to structural OH^- groups. It is worth noting that the intensity of this band was higher for all the apatites except for carbonate-rich apatites (Fig. 7). It was almost not detected in HapE-Na-CO_3 and was not so significant in the case of the HapE-CO_3 sample, confirming also the A-type substitution of OH^- by CO_3^{2-} ions in the carbonate-rich apatites.[40] So, the A-type substitution was especially evidenced when the carbonate content in the HAP was very high, which is in good agreement with the TGA results.

In brief, the IR spectra thus confirmed the A or/and B-type substitution by CO_3^{2-} groups in all the apatite solids, which is in agreement with the XRD and TGA observations.

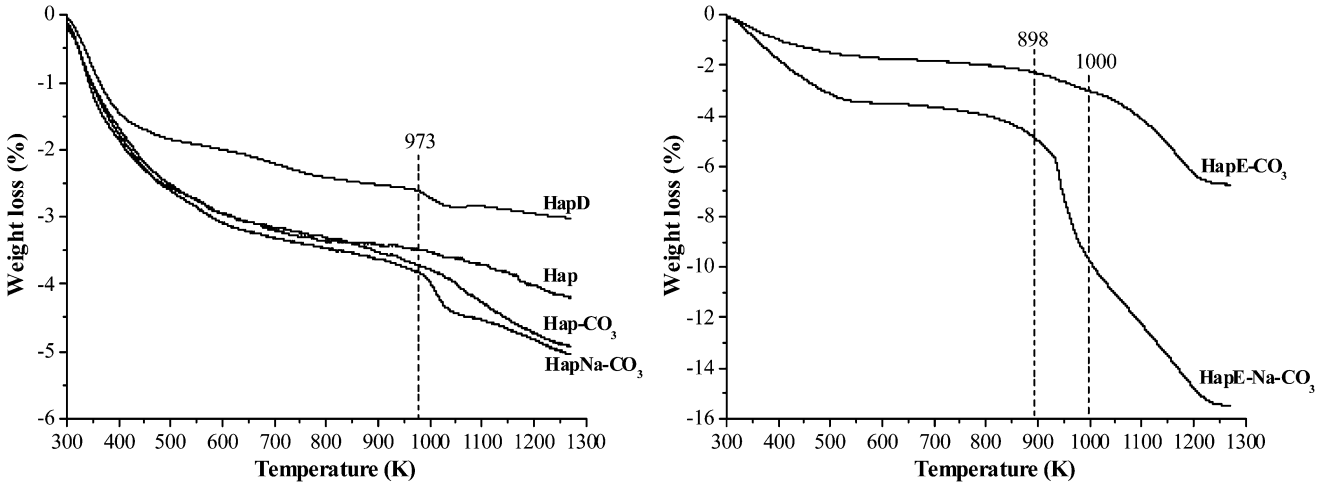

Fig. 4 TGA curves showing the weight loss of the samples calcined at 673 K. The derived curves of CO_2 loss obtained by using a mass spectrometer with $m/z = 44$ are shown in Fig. S5.†

Table 3 Carbonate mole content in the apatite solids of the general formula $Ca_{10-\delta}[(PO_4)_{6-x}(CO_3)_x][(OH)_y(CO_3)_z]$

Solids	CO_3^{2-} in the A sites from TGA (z)[a]	CO_3^{2-} in the B sites from TGA (x)[b]	CO_3^{2-} in the B sites from XRD (x)
HapD	—	0.14	0.18(5)
Hap	—	0.21[c]	0.32(5)
Hap-CO_3	—	0.40	0.37(5)
HapNa-CO_3	—	0.36[c]	0.37(6)
HapE-CO_3	0.30	0.83	0.64(9)
HapE-Na-CO_3	1.47	1.43	1.28(9)

[a] Deduced from the weight loss starting from 773 K. [b] Deduced from the weight loss starting from 973 K. [c] Underestimated since a plateau was not obtained.

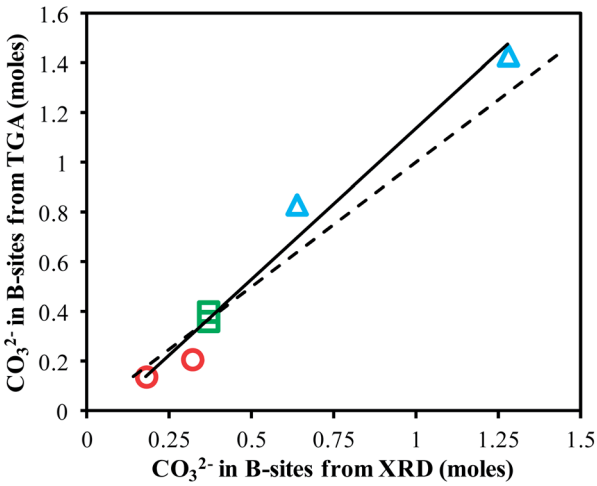

Fig. 5 Number of moles of CO_3^{2-} in B-sites obtained from TGA as a function of the same parameter obtained from XRD (circles represent HapD and Hap, squares for carbonated apatites, namely Hap-CO_3 and HapNa-CO_3, and triangles for carbonate-rich apatites, namely HapE-CO_3 and HapE-Na-CO_3). The dashed line represents the theoretical perfect correlation (1 to 1 ratio).

3.4 Presence of HPO_4^{2-} groups in the prepared solids

Since, it was not possible to clearly assess the presence of HPO_4^{2-} groups in the solids by using FTIR-spectroscopy, ^1H-^{31}P CP MAS-NMR was performed. This technique enables detecting the presence of P belonging to acidic HPO_4^{2-} groups and of P belonging to PO_4 (orthophosphate) species.

All the samples exhibited a common signal resonating at 3.3 ppm due to PO_4^{3-} species (Fig. S7†).[43] Moreover, the line shape of the peaks tended to vary with the carbonate content; carbonate-rich apatites give rise to broader peaks. This phenomenon is due to the distortions or defects in the P environment, resulting from the statistical carbonate substitution/removal of the ions in the apatite structure.[44] In addition to this signal, a broad peak centred at 6.5 ppm was clearly observed for HapD and Hap, which both contain a lower carbonate content compared to the other samples. For the other apatites, it was difficult to differentiate this signal due to its low intensity, and also because of the broadening of the signal of the orthophosphate species at 3.3 ppm. This peak can be attributed to a distribution of phosphorus species due to the low content of carbonate.

In order to confirm the presence of HPO_4^{2-} groups in the materials, 2D ^1H-^{31}P heteronuclear correlation (HETCOR) spectra were then recorded. Fig. 8 shows the 2D spectra of the solids at the short contact time of 1 ms, at which the intensity of the signal due to HPO_4^{2-} groups is known to be more pronounced than the phosphorus signal in the close vicinity of H_2O.[44] The 2D spectra of all the solids clearly show a signal resonating at 0 ppm along the ^1H axis due presence of the proton of OH^- that cross polarizes with P of phosphate groups, and a second signal resonating between 3 to 8 ppm along the ^1H axis mainly due to protons from HPO_4^{2-} groups. This latter is also observed in 2D spectra recorded with a very short contact time of 150 μs (not shown) corresponding to a selective time for a short P–O–H distance, hence to HPO_4^{2-} groups.[45]

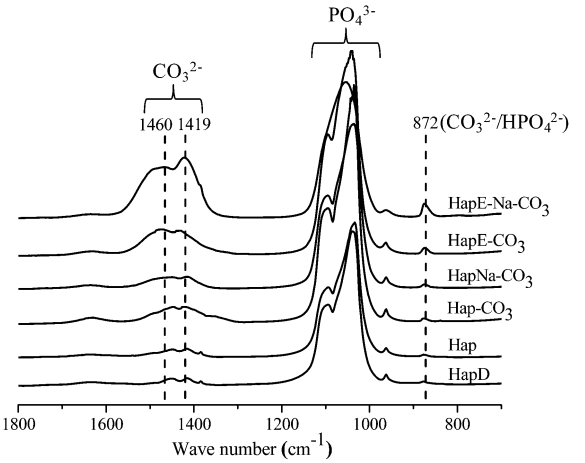

Fig. 6 IR spectra of HAPs in the 700–1800 cm^{-1} region.

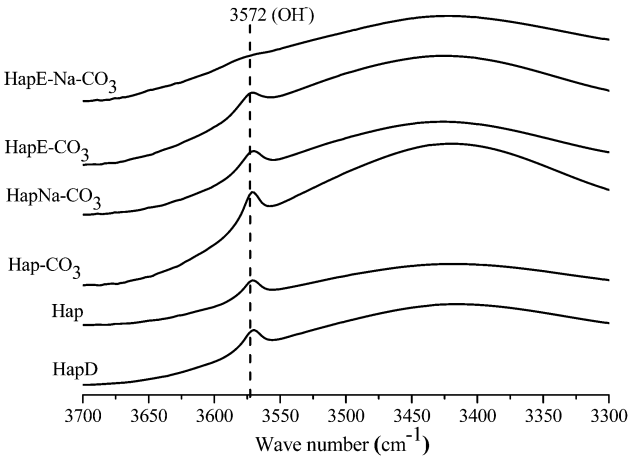

Fig. 7 IR spectra of HAPs in the 3300–3700 cm^{-1} region.

So, the presence of acidic HPO_4^{2-} groups was evidenced in all the HAPs, irrespective of the Ca/P ratio. However, quantification was not possible with this technique, which remains qualitative.

3.5 Surface composition of the HAPs

3.5.1 Surface Ca/P ratios and carbonate species. XPS analysis was then carried out to get surface information. The comparison of the Ca/P ratios and of the $C_{carbonates}$/P ratios determined by ICP, XRD/TGA and XPS is given in Table 4. Concerning the Ca/P ratios, the XPS surface analysis is in good agreement with the bulk analysis for all the solids, except for HapD and Hap. Surface Ca/P ratios of 1.19 in HapD and 1.27 in Hap were much lower than the bulk ratios, 1.62 and 1.69, respectively. This is in good agreement with previous studies,[3,46] and indicates that, for these two compositions, Ca species are less exposed to the surface than phosphates, at least within the *ca.* 10 nm analysis depth limit of the XPS technique. For the other samples, the surface Ca/P ratios increased from 1.66 (Hap-CO_3) to 2.06 (HapE-Na-CO_3) with the increase in the content of carbonate ions and turned out to be almost similar to bulk ratios.

The surface carbon-based species have been examined using the characteristics of the C 1s photopeak. The decomposition of the C 1s peak allowed us to evidence four components, corresponding namely to C–C, C–O and C=O bonds, as well as a specific feature corresponding to CO_3^{2-}, with respective binding energies of 285.0 (fixed reference), 286.5, 288.5 and 290.0 eV (Fig. S8†). The relative intensity of the peaks attributed to species containing C–O, C=O was similar, irrespective of the sample with C–O/C=O ratios between 1.2 and 1.8, whereas the intensity of the CO_3^{2-} species over the surface showed the global trend of increasing together with the CO_3^{2-} content (Table 4).

Previous studies have shown that a variation in the Ca/P ratio in HAPs drastically changes their chemical properties.[3] Likewise, the solids prepared with different Ca/P surface ratios, and, furthermore, exhibiting different $C_{carbonates}$/P ratios should exhibit different surface properties, depending in part on the amount of carbonates present on their surface – or, at least, adsorbable at their surface. This will be checked later on in the present paper when examining the acid–base properties of the solids.

As a partial conclusion for this part, while for all the samples the $C_{carbonates}$/P ratios obtained from XRD/TGA were comparable and in rather good agreement with the $C_{carbonates}$/P ratios obtained from ICP (Table 4), the $C_{carbonates}$/P ratio determined by XPS was not consistent, underlining the surface complexity in hydroxyapatite solids.

3.5.2 Composition of the outermost atomic layer of the samples. To get insights into the elemental composition in the first atomic layer of solids, LEIS, a very sensitive technique, is used. To verify whether the Ca/P ratio or the carbonate content affects the topmost surface atomic distribution, stoichiometric Hap (low Ca/P ratio and carbonate content) and HapE-Na-CO_3 (high Ca/P ratio and carbonate content) were chosen for analysis (Fig. 9). For Hap and HapE-Na-CO_3, two surface peaks due to Ca and O are clearly observed at 2000 eV and 1135 eV, respectively. A surface peak due to P is observed at 1790 eV, but is overlapped by the background signal resulting from the background of the secondary ions and/or the in-depth signal of Ca present from deeper layers. To clearly assess the expected position of a peak due to P, LEIS was performed using $NH_4H_2PO_4$ as a standard, which is a precursor used in the hydroxapatite synthesis. A signal is clearly observed at 1790 eV, thus confirming the presence of P on the apatite surfaces. Despite the poor intensity of the phosphorous peak, it is worth noting that it is less intense for HapE-Na-CO_3 than for Hap. These results suggest that Ca ions and O ions are more exposed to the first atomic layer of hydroxyapatites, irrespective of the Ca/P ratio (1.69 & 2.39) and of the carbonate content (0.40 & 2.95 wt%) in Hap and HapE-Na-CO_3, respectively. This may contradict the results obtained by XPS, which showed a lower Ca/P ratio for Hap. However, we have to remind that the LEIS technique only probes the topmost atomic layer of the samples, while XPS gives information on the composition, but along a depth of a few nanometers. The O atoms of the first atomic layer belong to PO_4^{3-}, CO_3^{2-} and CaO/

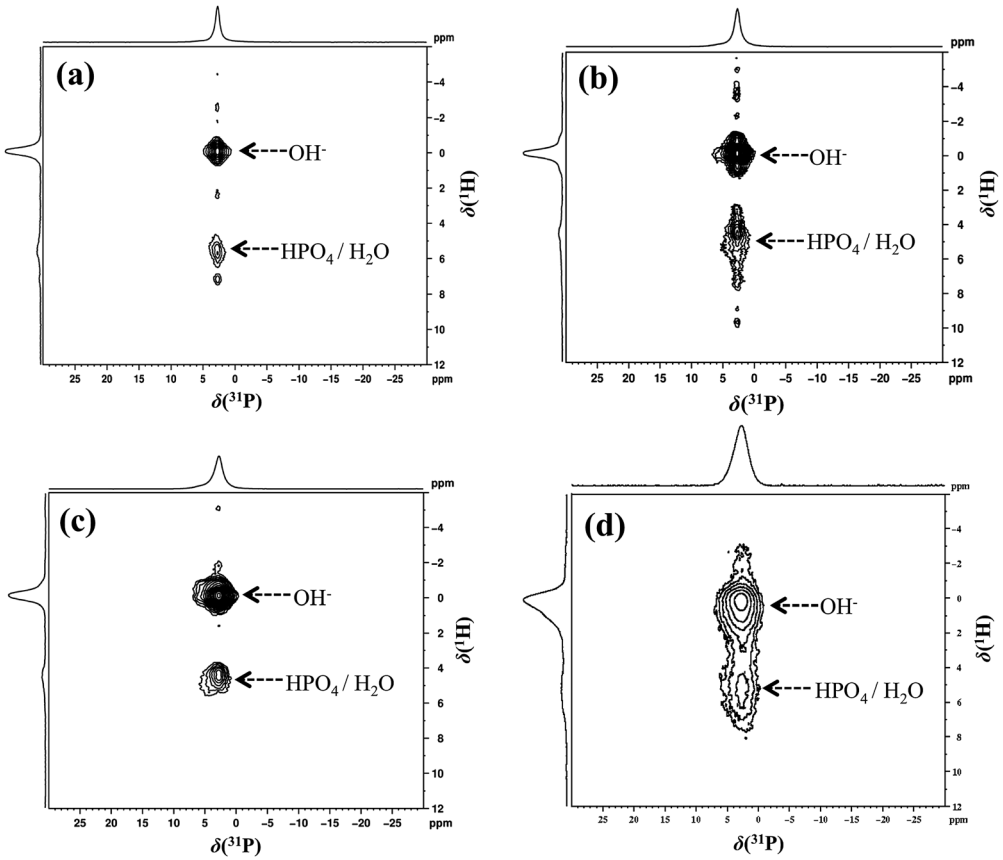

Fig. 8 2D HETCOR spectra of (a) HapD, (b) Hap, (c) HapNa-CO_3, and (d) HapE-Na-CO_3.

Table 4 Comparison of Ca/P & $C_{carbonates}$/P atomic ratios in the apatites determined by ICP, XRD, TGA & XPS

Solid	ICP Ca/P atomic ratio	XRD Ca/P atomic ratio (% difference relative to ICP)	XPS Ca/P atomic ratio (% difference relative to ICP)	ICP $C_{carbonates}$/P atomic ratio	XRD-TGA $C_{carbonates}$/P atomic ratio	XPS $C_{carbonates}$/P atomic ratio
HapD	1.62	1.71 (+5.5%)	1.19 (−26.5%)	0.03	0.02	0.07
Hap	1.69	1.76 (+4.1%)	1.27 (−24.9%)	0.06	0.04[a]	0.10
Hap-CO_3	1.70	1.77 (+4.1%)	1.66 (−2.4%)	0.09	0.07	0.21
HapNa-CO_3	1.72	1.78 (+4.7%)	1.67 (−2.9%)	0.10	0.06[a]	0.14
HapE-CO_3	1.90	1.86 (−2.1%)	1.81 (−4.7%)	0.22	0.21	0.14
HapE-Na-CO_3	2.39	2.12 (−11.3%)	2.06 (−13.8%)	0.59	0.61	0.23

[a] Underestimated since a plateau was not obtained.

Ca–O^- species present at the surface of the apatites. So, we could also propose that the surface of the hydroxyapatite crystallites mainly consists of Ca species rather than P species. Since the results obtained from Rietveld refinements have shown that the crystallite growth is more along the [0 0 1] direction or in the *c*-axis direction, the Ca ions should be more exposed along the *c*-axis, that is, on *ac* and *bc* planes. A schematic representation of the two possible crystallite surface cleavages is shown in Fig. 10. According to the above results, we then suppose that, in our study, the apatite crystallites are mainly cleaved in such a way that Ca atoms are more exposed on the surface, represented by the green line in Fig. 10.

3.6 Acid–base properties of the solids

3.6.1 Acid site number, nature, and relative distribution. Fig. 11 shows the NH_3-TPD curves for all the apatite solids. It clearly appears that the peak corresponding to the deficient apatite HapD is much broader and exhibits the highest Full Width at Half Maximum (FWHM) value of 497 K. In addition, the maximum of the peak of HapD was shifted to a higher desorption temperature (513 K) compared to the other solids. This reflects the presence of stronger acid sites in a very broad temperature range extending up to 773 K. The FWHM decreased further to 435 K for Hap, whose peak is broadened up to a

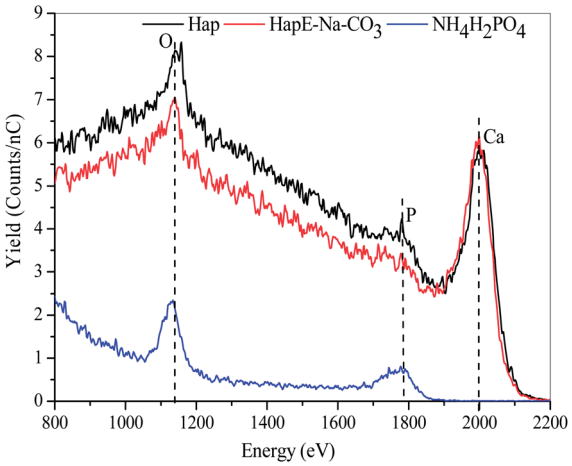

Fig. 9 LEIS spectra of selected apatite solids.

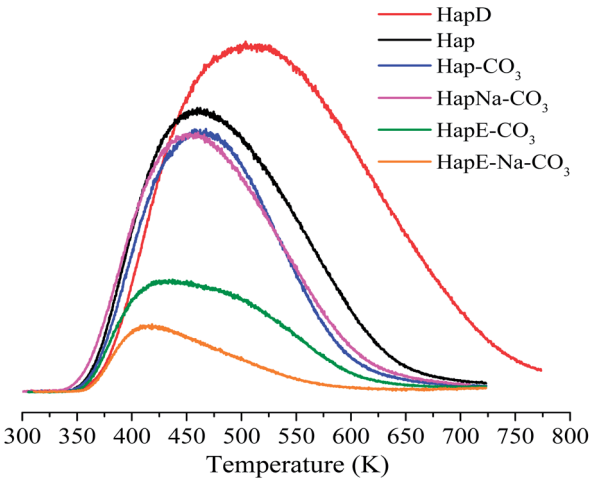

Fig. 11 NH_3-TPD curves of the apatite solids.

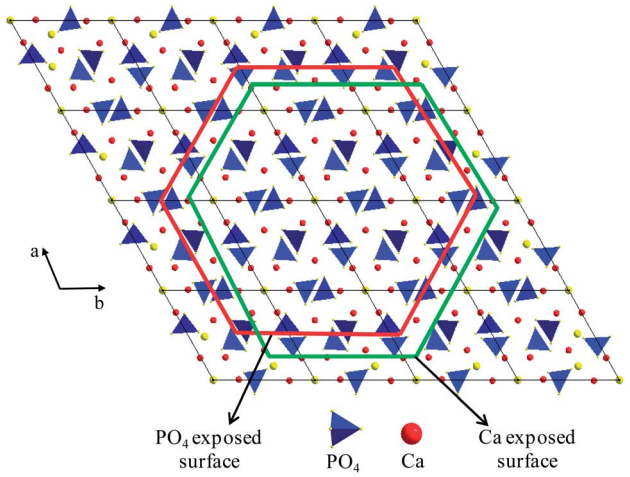

Fig. 10 Schematic representation of the hydroxyapatite lattice: the green line shows the crystallite surface cleavage through Ca atoms, which actually occurrs according to our study, and the red line shows the theoretical crystallite cleavage through P atoms that is another possibility, but not predominant in our solids.

desorption temperature of 698 K. The FWHM was lowered for carbonated apatites Hap-CO_3 (410 K) and HapNa-CO_3 (412 K) compared to more acidic apatites HapD and Hap, but these samples still possessed acid sites of a relatively high strength, of which the desorption temperature extended up to 623 K. The intensity of the signals obtained for carbonate-rich apatites was clearly lower compared to that of the other apatites, though the desorption temperature extended up to 623 K, similarly to that of the carbonated apatites. Hence, Hap and especially HapD show their predominant acidic character with stronger acid sites compared to other apatites.

The total number of acid sites in the samples was determined by integrating the NH_3-TPD profiles and the results are gathered in Table 5. The specific acidity of the apatites decreased rather linearly from 7.73 to 1.87 μmol m^{-2} with the increase in the Ca/P surface ratio and the surface carbonate content, as shown in Fig. S9.† The variation in the specific acidity can be linked with many parameters, such as the crystallite morphology, the surface Ca/P ratio, and the quantity of surface HPO_4^{2-}, CO_3^{2-}, CaO species, resulting from the replacement of PO_4^{3-}/OH^- groups.[3,46] It has been observed from LEIS that Ca^{2+} (Lewis acid sites) present in *ac* and *bc* unit cell faces of apatites become more exposed to the surface if crystallite grows along the [0 0 1] direction, which is in good agreement with previous reports.[47,48]

We saw above that the crystallite growth along the *c*-axis ([0 0 1] direction) increased with the carbonate content, which means that the carbonate-rich apatites, which have a larger crystallite size along the *c*-axis, should possess more acid sites due to the exposure of a larger amount of Ca^{2+} species. Instead, carbonate-rich apatites presented a lower density in acid sites, maybe because most of the Ca exists in the form of CaO or Ca–O^- species present at the surface due to the excess Ca/P ratio in carbonate-rich apatite solids. The Ca $2p_{3/2}$ XPS peak of carbonate-rich apatites was broadened with higher FWHM compared with the peak of stoichiometric Hap (data not shown), most probably due to the presence of CaO. Moreover, the high temperature XRD showed peaks due to CaO species, which are more predominant in carbonate-rich apatites. So, we suppose that the CaO phase might also be present in all the apatite solids at room temperature, but in a highly dispersed – surface – state, similar to recent findings on Sr apatites, which evidenced the presence of highly dispersed SrO species.[49] HapD has a higher number of acid sites due to the contribution from HPO_4^{2-} groups or OH^- vacancies, which are more numerous in deficient apatites and in good agreement with previous reports.[3]

PEA-XPS investigation of the apatite surfaces was used as a complementary way to the TPD approach to determine the Brønsted or Lewis nature of the surface acid sites, as previously reported.[22,50] The PEA-XPS spectra of all the samples presented a broad N 1s peak centered at binding energies in the 396.5–405.0 eV range, which could be decomposed into two peaks, at BEs of 398.0–405.0 eV and 396.5–403.5 eV, thus revealing the presence of Brønsted and Lewis acid sites, respectively (Fig. 12). Also, it has been reported that the basic probe can be retained on

Table 5 Number, nature and distribution of acid sites determined by NH_3-TPD and PEA-XPS

Solids	Number of acid sites (μmol g^{-1})	Specific acidity (μmol m^{-2})	Nature & distribution of acid sites: Lewis (μmol m^{-2})	Nature & distribution of acid sites: Brønsted (μmol m^{-2})
HapD	956	7.73	5.16 (66.7%)	2.57 (33.3%)
Hap	763.3	6.73	5.43 (80.7%)	1.30 (19.3%)
Hap-CO_3	658	6.13	5.58 (91.1%)	0.54 (8.9%)
HapNa-CO_3	604	5.53	5.17 (93.5%)	0.36 (6.5%)
HapE-CO_3	324	4.27	4.01 (94%)	0.26 (6%)
HapE-Na-CO_3	141.3	1.87	1.78 (95.3%)	0.09 (4.7%)

Brønsted sites by the formation of an ammonium cation and on Lewis sites by the formation of a complex.[22,50] Taking into account the hydroxyapatite surface, we propose that the ammonium cation can be formed with PEA mainly on acidic HPO_4^{2-} groups present on the HAP surface and the complex formation can take place over Ca^{2+} or over OH^- vacancies (δ+) (Fig. 13).

Hence, in all the HAPs, HPO_4^{2-} groups act as Brønsted acid sites and Ca^{2+}/vacancies as Lewis acid sites. The obtained relative distribution of Lewis and Brønsted acid sites is reported in Table 5 together with the specific amount of each site.

Irrespective of the sample, the contribution of the Lewis acid sites was dominant and varied between 66.7% and 95.3%. PEA-XPS showed that all the solids possess Brønsted HPO_4^{2-} groups irrespective of the Ca/P ratio, which is in good agreement with the 2D-NMR results. More HPO_4^{2-} groups present in HapD resulted in the presence of more Brønsted sites, when compared to the other samples. Contribution from Brønsted HPO_4^{2-} groups was lower in carbonate-rich HAPs compared with the other solids, which supposedly results from the substitution of OH^-/PO_4^{3-} by the CO_3^{2-} group, required to counterbalance the charge.[47] For carbonate-rich apatites, there is also an observable decrease in the number of Lewis acid sites (Ca^{2+}) compared to the other apatites, though they possess higher Ca/P ratios compared to the other apatites. This decrease in the number of Lewis acid sites can be due to the formation of CaO species over the carbonate-rich apatites, which are no more Lewis acid sites, but consequently leave basic sites on the surface.

Hence, the HapD and Hap have much more contribution of 33.3% and 19.3%, respectively, from the Brønsted acid sites compared to all the other apatites, whose Brønsted acid site contribution varies between 4.7% (HapE-Na-CO_3) and 8.9% (Hap-CO_3). For HapD and Hap, this larger contribution of Brønsted acid sites is linked with the observation of higher FWHMs of 497 K and 435 K, respectively, of their NH_3-TPD profiles, so that we can deduce that, on these samples, strong Brønsted acid sites are created.

3.6.2 Number and distribution of basic sites. Basic sites with at least three different strengths can be distinguished from the CO_2-TPD profiles (Fig. 14). The main contribution to the CO_2 desorption peak seems to be due to weak basic sites with a maximum observed at 398 ± 10 K over all the apatites. A second peak at around 493 K due the presence of basic sites of a medium strength is also observed, more clearly for HapNa-CO_3 and Hap-CO_3 with a more intense signal. A last peak is observed at around 613 K, due to the presence of strong basic sites for Hap, Hap-CO_3 and HapNa-CO_3. This peak was observed neither in the deficient apatite HapD nor in the carbonate-rich apatites (HapE-CO_3 and HapE-Na-CO_3). Since the carbonate-rich apatites are solids that have shown the A-type substitution of CO_3^{2-} replacing the OH^- groups, we suppose that the absence of the peak due to stronger basic sites arises from the lack in basic OH^- species. It is known that in the case of deficient apatites (here, HapD), deficiency of Ca^{2+} ions is compensated by the addition of H^+ and removal of OH^- ions, and this may be the reason for the absence of OH^- peaks in HapD. But, further investigations are needed to confirm this assumption of OH^- as stronger basic sites.

The amount of basic sites was determined by integrating the TPD profile of CO_2 (Table 6). The number of basic sites tended to increase from 41.33 μmol g^{-1} to 155.33 μmol g^{-1} when the Ca/P ratio or the carbonate content increased from HapD to HapNa-CO_3, and then decreased with further increase in the Ca/P ratio or carbonate content in carbonate rich apatites.

In contrast, the specific basicity increased from 0.33 μmol m^{-2} to 1.4 μmol m^{-2} when the Ca/P ratio or the carbonate content increased from HapD to HapNa-CO_3 and remained almost unchanged with further increase in the Ca/P ratio, namely in carbonate-rich apatites, HapE-CO_3 and HaE-Na-CO_3.

Benzoic acid adsorption using a pulse liquid chromatographic technique,[23] a complementary technique to TPD-CO_2, was also employed to determine the distribution of strong and weak basic sites. Specific basicity determined by benzoic acid adsorption show somewhat different results compared to the TPD-CO_2 technique. Contrary to the lower amount of basic sites in HapD (0.33 μmol m^{-2}) compared with Hap (0.87 μmol m^{-2}) as determined by TPD-CO_2, the benzoic acid adsorption resulted in higher amounts of basic sites in HapD (2.09 μmol m^{-2}) than in stoichiometric Hap (1.70 μmol m^{-2}). Considering the carbonated apatites, Hap-CO_3 owns specific basic sites of 4.66 μmol m^{-2}, but HapNa-CO_3 (1.24 μmol m^{-2}) has the lowest amount of specific basic sites compared to all the other apatites. Specific basicity observed for carbonate-rich apatites HapE-CO_3 (4.08 μmol m^{-2}) and HapE-Na-CO_3 (4.88 μmol m^{-2}) were higher than for all the other apatites except for Hap-CO_3, which has more basic sites than HapE-CO_3. The highest amount of basic

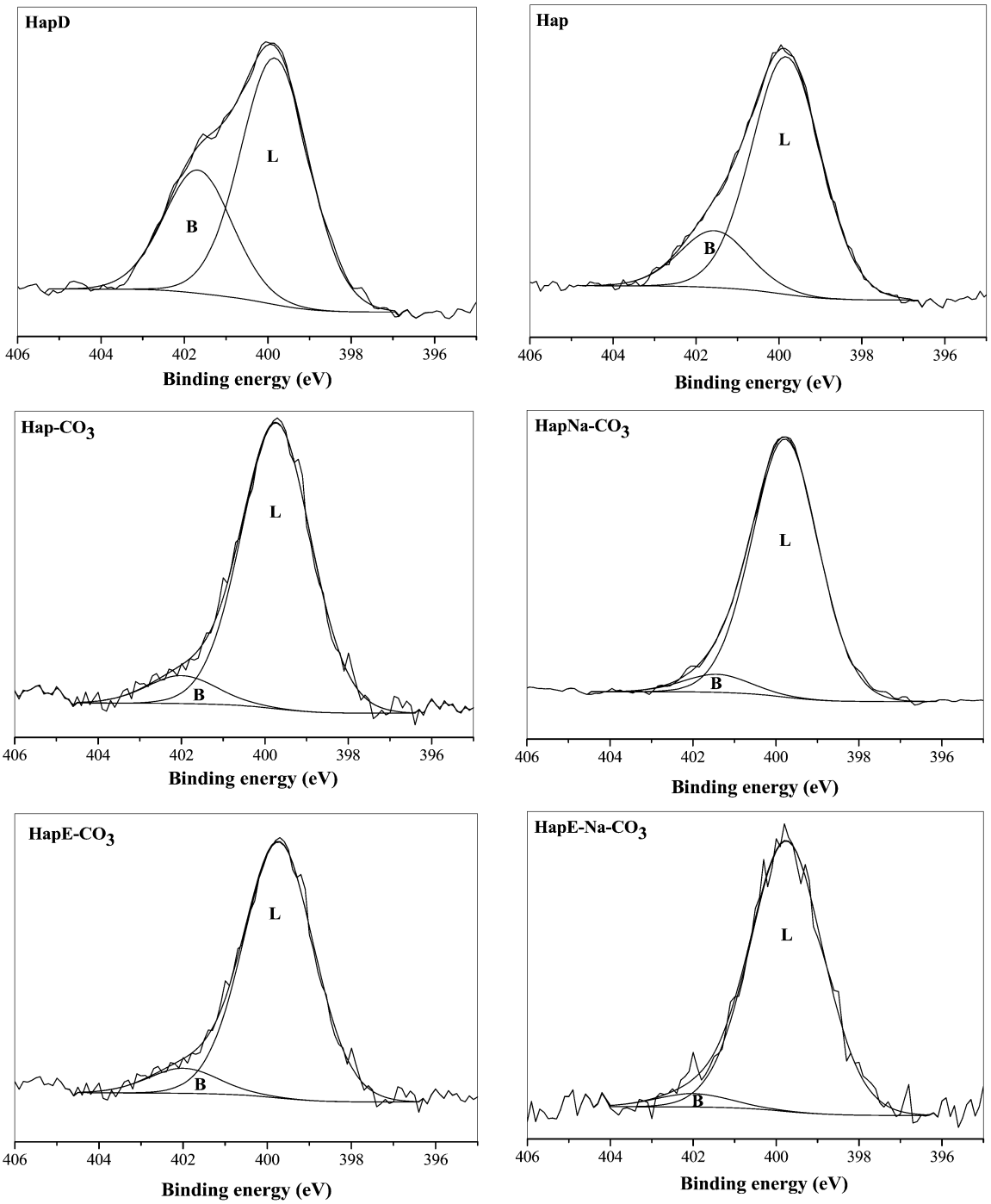

Fig. 12 Decomposition of the N 1s photopeak after PEA adsorption on the apatite solid surface.

sites obtained using benzoic acid determination once again confirms the presence of CaO species in carbonate-rich apatites.

3.6.3 Acid–base reactivity of the HAPs. Isopropanol tests were performed at an isopropanol conversion of 20% and the variation in propylene and acetone distribution over the HAPs is shown in Fig. 15. The catalytic conversion of isopropanol over all the apatites yielded propylene, acetone, di-isopropyl ether and negligible amount of dienes. Acetone can be formed over basic sites and propylene and di-isopropyl ether over acid sites, as previously reported. The propylene formation was much higher over HapD and Hap compared to all the other apatites, underlining the acidic behavior of these catalysts, which is in good agreement with TPD-NH_3 and PEA-XPS. The high amount of acid sites and the presence of more Brønsted acid sites (HPO_4^{2-} groups) with higher strength in HapD and Hap can explain this predominant formation of propylene. The propylene selectivity was lowered from 92% to 40.3% with increase in the Ca/P ratio from 1.62 in HapD to 1.69 in Hap, but

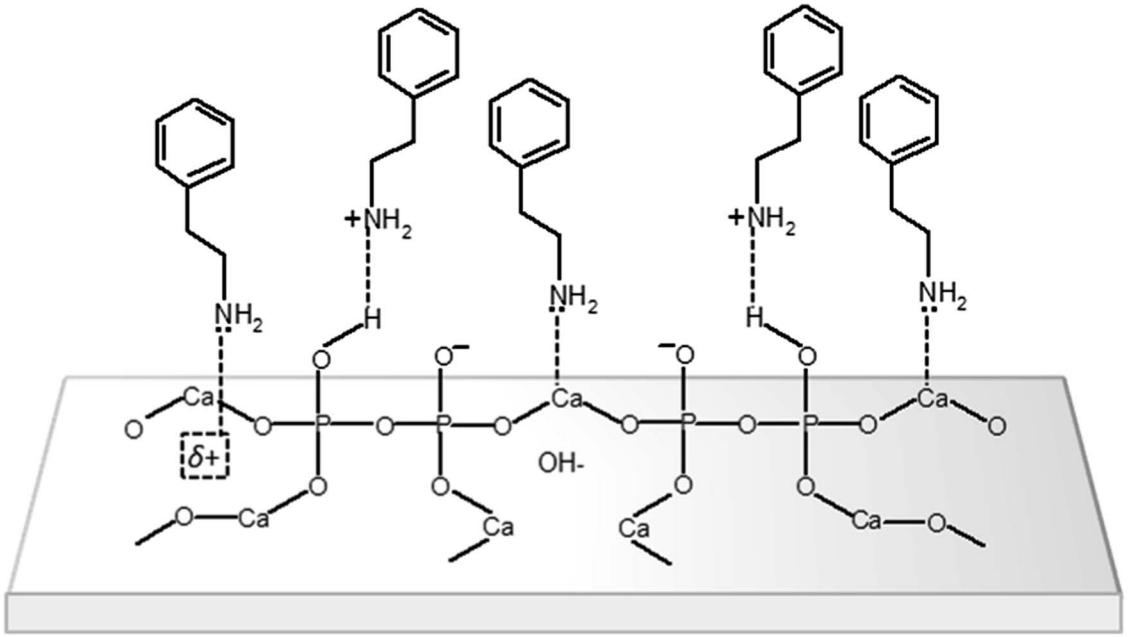

Fig. 13 Model of PEA adsorption over Lewis and Brønsted acid sites on the surface of apatites [(δ+) = OH^- vacancies].

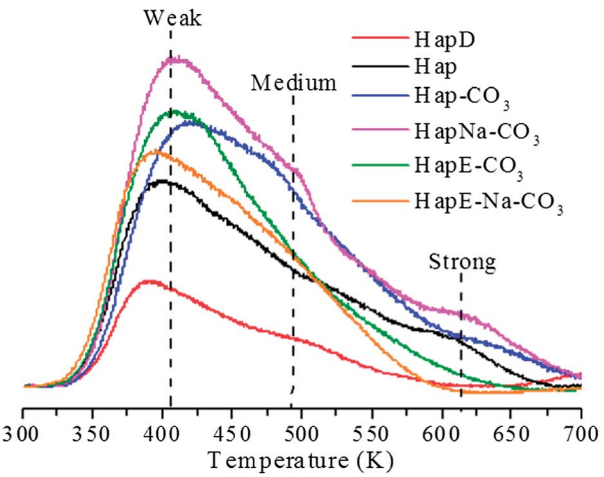

Fig. 14 CO_2-TPD profiles of the apatite solids.

Hap still possessed a relatively high acidic character compared to the other catalysts. For carbonated apatites, Hap-CO_3 (Ca/P = 1.70) and HapNa-CO_3 (Ca/P = 1.72), the propylene formation was then drastically reduced to 7% and 8.4%, respectively. This shows decrease in the acidic behaviour of HAPs with increase in the Ca/P ratio or the carbonate amount above a certain limit. Selectivity to propylene was further lowered to 3.5% and 4.2%, respectively for carbonate-rich apatites HapE-CO_3 (Ca/P = 1.90) and HapE-Na-CO_3 (Ca/P = 2.39), showing the lack in acidic nature of apatites with very high Ca/P ratios or carbonate contents.

Selectivity to acetone tended to increase readily with the increase in the Ca/P ratio from HapD to HapE-Na-CO_3. HapD with the lower Ca/P ratio of 1.62 was less selective to acetone (5%) than all the other apatites, which is in good agreement with the lower number of basic sites (41.33 μmol g^{-1}) over this sample. Selectivity to acetone considerably increased to 39% in Hap (Ca/P = 1.69). Further increase in the Ca/P ratio for carbonated apatites, namely Hap-CO_3 and HapNa-CO_3, led to an

Table 6 Basic site distribution determined by TPD-CO_2 and benzoic acid adsorption

		TPD-CO_2		Benzoic acid adsorption			
Solids	Ca/P atomic ratio (ICP)	Total basic sites (μmol g^{-1})	Specific basicity (μmol m^{-2})	Total basic sites (μmol g^{-1})	Specific basicity (μmol m^{-2})	Strong basic sites (μmol m^{-2})	Weak basic sites (μmol m^{-2})
HapD	1.62	41.33	0.33	259.9	2.09	1.88	0.21
Hap	1.69	100.67	0.87	194.3	1.70	1.45	0.25
Hap-CO_3	1.70	136	1.27	499.5	4.66	4.66	0
HapNa-CO_3	1.72	155.33	1.4	134.7	1.24	0.83	0.41
HapE-CO_3	1.90	112.67	1.47	310.4	4.08	3.60	0.48
HapE-Na-CO_3	2.39	104	1.47	351.6	4.88	4.29	0.59

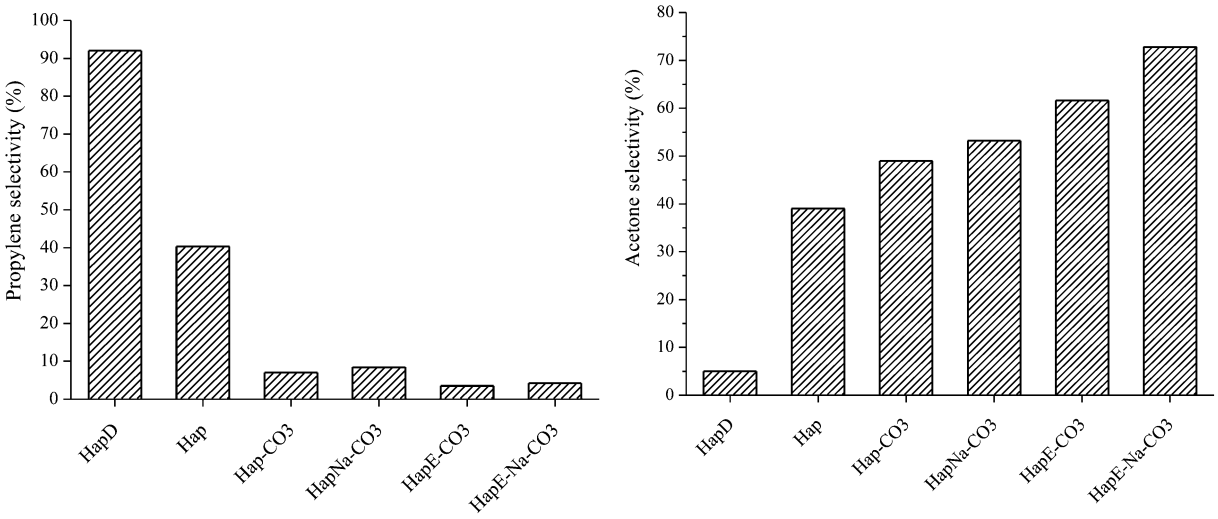

Fig. 15 Selectivity to propylene and acetone at 20% conversion of isopropanol in the presence of the apatite solids.

increase in the acetone selectivity to 49%, and 53.2%, respectively. While the carbonate-rich solids, HapE-CO_3 (Ca/P = 1.90) and HapE-Na-CO_3 (Ca/P = 2.39) possess a lower number of basic sites compared to carbonated apatites, they have shown higher selectivity to acetone compared to all the other apatites. This can be due to the presence of more basic CaO species over carbonate-rich apatites, which enhance the dehydrogenation of isopropanol to acetone. Comparing the carbonate-rich apatites HapE-CO_3 and HapE-Na-CO_3, the latter was found to be more selective to acetone, though it possesses a lower amount of basic sites compared to HapE-CO_3. This can be thus due to formation of more CaO species over HapE-Na-CO_3 compared to HapE-CO_3. It is also worth noting that, though catalysts Hap, Hap-CO_3 and HapNa-CO_3 possess stronger basic sites, they have shown lower selectivity to acetone compared to carbonate-rich apatites, which lack in stronger basic sites. This might indicate that dehydrogenation of isopropanol to acetone probably mainly took place over weak or medium basic sites.

The plot of the propylene/acetone selectivity ratio (indirectly representing the acid/base behavior) as a function of the number of acid sites to the number of basic sites (direct acid–base behavior) is shown in Fig. 16. Hap and HapD clearly show a deviation (represented by dashed line) from the other apatites, which can be related to their higher acidic behavior (Fig. 16(a)). In addition, a rather linear increase in the propylene/acetone selectivity ratio with the acidity/basicity ratio (dashed line in Fig. 16(b)) was observed for carbonated and carbonate-rich apatites. Then, a remarkable correlation is observed between the isopropanol reactivity and acid–base properties for these samples.

Formation of di-isopropyl ether was observed in small amounts, 2% in HapD and 0.9% in Hap and trace amounts (below the quantification limit of *ca.* 0.5%, with a slightly visible GC peak quite mixed with the background and thus not exploitable) over the other apatites.

As a conclusion to this part, HapD and Hap have shown their predominant acidic behaviour compared to all the other

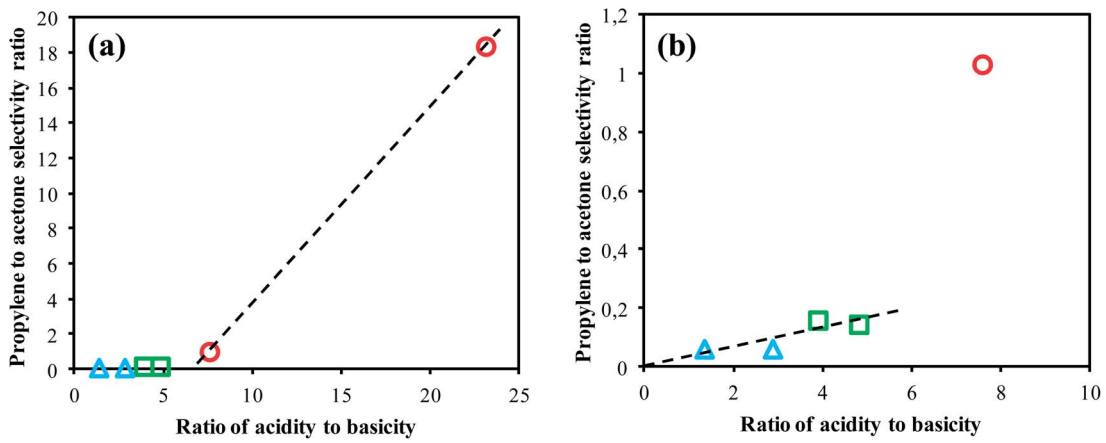

Fig. 16 (a) Ratio of propylene to acetone selectivity as a function of the ratio between the number of acid sites to the number of basic sites and (b) the same figure focused on a narrower range of the acidity/basicity ratio (red circles representing HapD and Hap, green squares for carbonated apatites, namely Hap-CO_3 and HapNa-CO_3, and blue triangles for carbonate-rich apatites, namely HapE-CO_3 and HapE-Na-CO_3).

apatites, which have shown much lower propylene selectivities. This predominant acidic behaviour is mainly due to the presence of stronger acid sites, especially of the Brønsted type. The presence of highly dispersed basic CaO species created from excess the Ca/P ratio than the stoichiometric value (1.67) could be the reason for the higher acetone selectivity over carbonate-rich apatites. Also, the results suggest that dehydrogenation of isopropanol to acetone takes place over weak and medium basic sites – and not over the stronger basic sites.

Conclusions

Hydroxyapatites with different Ca/P ratios were successfully synthesized using a precipitation method, optionally containing also Na^+ cations, and were extensively characterized.

Their carbonate content increased linearly with the Ca/P ratio. The occupancy of atoms was calculated using Rietveld refinement, and the so-obtained (Ca + Na)/P ratios were in good agreement with those obtained from ICP. A good correlation was further observed between the anisotropic crystallite shape obtained from XRD and the grain shape observed in SEM. Global tentative formulae for the apatites were deduced from the amount of CO_3^{2-} substituted in the OH^- sites (A-type) and the PO_4^{3-} sites (B-type): $(Ca_{10-\delta}[(PO_4)_{6-x}(CO_3)_x][(OH)_y(CO_3)_z])$. LEIS showed that Ca^{2+} is more exposed at the topmost surface of the apatite solids, irrespective of the Ca/P ratio. Combining the results of XRD refinement and LEIS, we proposed that Ca^{2+} are more exposed along the (0 0 1) direction on the *ac* and *bc* planes. The presence of HPO_4^{2-} entities suggested by IR spectra was confirmed in all the apatites using 2D NMR (HETCOR sequence). Further, PEA-XPS proved that HPO_4^{2-} species act as Brønsted acid sites, and Ca^{2+} or OH^- vacancies (δ^+) as Lewis acid sites. The acid–base reactivity of the solids was subsequently determined using isopropanol reactivity, which gave selectivity results is in good agreement with the acid–base properties directly obtained using NH_3-TPD, PEA-XPS, and CO_2-TPD. As a remarkable feature, HapD (deficient apatite) and Hap (stoichiometric apatite) showed a much more pronounced acidic behavior than that of the other apatites.

Further, the solids presented in the present study were used in the Guerbet reaction, which requires the presence of both acidic and basic sites, and showed different reactivities in agreement with the results of the present paper.[51]

Acknowledgements

The research leading to these results has received funding from the European Union Seventh Framework Programme (FP7/2007-2013) under grant agreement no. 241718 EuroBioRef. The "Fonds Européen de Développement Régional (FEDER)", "CNRS", "Région Nord-Pas-de-Calais" and "Ministère de l'Education Nationale de l'Enseignement Supérieur et de la Recherche" are acknowledged for fundings of X-ray diffractometers, NMR spectrometers and the regional platform of surface analysis. The French-Italian research project PHC Galilée no 25955PK (2011–2012) is acknowledged for its financial support. The authors also want to warmly thank Dr Arnaud Beaurain and Mrs Martine Trentesaux for their technical help on XPS spectra recording, Dr Franco Finol for his help on PEA-XPS experiments, and, finally, Mr Olivier Gardoll for his technical help on NH_3-TPD and TGA experiments.

Notes and references

1 J. C. Eliott, *Structure and Chemistry of the Apatites and Other Calcium Orthophosphates*, Elsevier, Amsterdam, 1994.
2 S. Koutsopoulos, Synthesis and characterization of hydroxyapatite crystals: A review study on the analytical methods, *J. Biomed. Mater. Res.*, 2002, **62**, 600–612.
3 T. Tsuchida, J. Kubo, T. Yoshioka, S. Sakuma, T. Takeguchi and W. Ueda, Reaction of ethanol over hydroxyapatite affected by Ca/P ratio of catalyst, *J. Catal.*, 2008, **259**, 183–189.
4 L. C. Kibby and K. W. Hall, Studies of acid catalyzed reactions: XII. Alcohol decomposition over hydroxyapatite catalysts, *J. Catal.*, 1973, **29**, 144–159.
5 S. J. Joris and C. H. Amberg, Nature of deficiency in nonstoichiometric hydroxyapatites I. Catalytic activity of calcium and strontium hydroxyapatites, *J. Phys. Chem.*, 1971, **75**, 3167–3171.
6 T. Tsuchida, S. Sakuma, T. Takeguchi and W. Ueda, Direct Synthesis of n-Butanol from Ethanol over Nonstoichiometric Hydroxyapatite, *Ind. Eng. Chem. Res.*, 2006, **45**, 8634–8642.
7 A. Sohly, R. Tahir, S. Sebti, R. Skouta, M. Bousmina, M. Zahouily and M. Larzek, Efficient synthesis of chalcone derivatives catalyzed by re-usable hydroxyapatite, *Appl. Catal., A*, 2010, **374**, 189–193.
8 S. Sebti, R. Tahir, R. Nazih and S. Boulaajaj, Comparison of different Lewis acid supported on hydroxyapatite as new catalysts of Friedel-Crafts alkylation, *Appl. Catal., A*, 2001, **218**, 25–30.
9 C. L. Kibby and K. W. Hall, Dehydrogenation of alcohols and hydrogen transfer from alcohols to ketones over hydroxyapatite catalysts, *J. Catal.*, 1973, **31**, 65–73.
10 N. Cheikhi, M. Kacimi, M. Rouimi, M. Ziyad, L. F. Liotta, G. Pantaleo and G. Deganello, Direct synthesis of methyl isobutyl ketone in gas-phase reaction over palladium-loaded hydroxyapatite, *J. Catal.*, 2005, **232**, 257–267.
11 T. J. Webster, E. A. Massa-Schlueter, J. L. Smith and B. E. Slamovich, Osteoblast response to hydroxyapatite doped with divalent and trivalent cations, *Biomaterials*, 2004, **25**, 2111–2121.
12 S. Shimoda, T. Aoba, E. Morenoe and Y. Miake, Effect of Solution Composition on Morphological and Structural Features of Carbonated Calcium Apatites, *J. Dent. Res.*, 1990, **69**, 1731–1740.
13 T. S. B. Narasaraju and D. E. Phebe, Some physico-chemical aspects of hydroxylapatite, *J. Mater. Sci.*, 1996, **31**, 1–21.
14 S. Kannan, J. H. G. Rocha and J. M. F. Ferreira, Synthesis and thermal stability of sodium, magnesium co-substituted hydroxyapatites, *J. Mater. Chem.*, 2006, **16**, 286–291.
15 S. Sugiyama, T. Osaka, Y. Ueno and K.-I. Sotowa, Oxidative Dehydrogenation of Propane over Vanadate Catalysts

Supported on Calcium and Strontium Hydroxyapatites, *J. Jpn. Pet. Inst.*, 2008, **51**, 50–57.
16 St. Naray-Szabo, *Z. Kristallogr.*, 1930, **75**, 387–398.
17 M. Mehmel, *Z. Kristallogr.*, 1930, **75**, 323–331.
18 J. C. Elliott, R. M. Wilson and S. E. P. Dowker, JCPDS-International Centre for Diffraction Data, Advances in X-ray Analysis, 2002, vol. 45.
19 N. S. Resende, M. Nele and V. M. M. Salim, Effect of anion substitution on the acid properties of hydroxyapatite, *Thermochim. Acta*, 2006, **451**, 16–21.
20 T. Kawasaki, S. Takahashi and K. Ikeda, Hydroxyapatite high-performance liquid chromatography: column performance for proteins, *Eur. J. Biochem.*, 1985, **152**, 361–371.
21 K. Kandori, T. Shimizu, A. Yasukawa and T. Ishikawa, Adsorption of bovine serum albumin onto synthetic calcium hydroxyapatite: influence of particle texture, *Colloids Surf., B*, 1995, **5**, 81–87.
22 A. Gervasini, A. Auroux and C. Guimon, Acidic Character of Metal-Loaded Amorphous and Crystalline Silica-Aluminas determined by XPS and Adsorption Calorimetry, *J. Phys. Chem. B*, 1999, **103**, 7195–7205.
23 P. Carniti, A. Gervasini and S. Biella, Determination of Catalyst Surface Acidity in Liquids by a Pulse Liquid Chromatographic Technique, *Adsorpt. Sci. Technol.*, 2005, **23**, 739–749.
24 C. Lamonier, J.-F. Lamonier, B. Aellach, A. Ezzamarty and J. Leglise, Specific tuning of acid/base sites in apatite materials to enhance their methanol thiolation catalytic performances, *Catal. Today*, 2011, **164**, 124–130.
25 J. Rodriguez-Carjaval, Recent Developments of the Program FULLPROF, in *Commission on Powder Diffraction*, International Union of Crystallography (IUCr) Newsletter, No. 26, 2001, pp. 12–19.
26 P. Thomson, D. E. Cox and J. B. Hastings, Rietveld Refinement of Debye-Scherrer Synchrotron X-ray Data from Al_2O_3, *J. Appl. Crystallogr.*, 1987, **20**, 79–83.
27 S. Raynaud, E. Champion, D. Bernache-Assollant and P. Thomas, Calcium phosphate apatites with variable Ca/P atomic ratio I. Synthesis, characterization and thermal stability of powder, *Biomaterials*, 2002, **23**, 1065–1072.
28 B. Aellach, A. Ezzamarty, J. Leglise, C. Lamonier and J.-F. Lamonier, Calcium-deficient and stoichiometric hydroxyapatites promoted by Cobalt for the catalytic removal of oxygenated Volatile Organic Compounds, *Catal. Lett.*, 2010, **135**, 197–206.
29 J. M. Hughes, M. Cameron and K. D. Crowley, Structural variations in natural F, OH and Cl apatites, *Am. Mineral.*, 1989, **74**, 870–876.
30 M. Jarvinen, Application of symmetrized harmonics expansion to correction of the preferred orientation effect, *J. Appl. Crystallogr.*, 1993, **26**, 525–531.
31 J. F. Berar and P. Lelann, E.s.d.'s and estimated probable error obtained in Rietveld refinements with local correlations, *J. Appl. Crystallogr.*, 1991, **24**, 1–5.
32 A. Krajewski, M. Mazzochi, P. L. Buldini, A. Ravaglioli, A. Tinti, P. Taddei and C. Fagnano, Synthesis of carbonated hydroxyapatites: efficiency of the substitution and critical evaluation of analytical methods, *J. Mol. Struct.*, 2005, **744**, 221–228.
33 R. M. Wilson, J. C. Elliott, S. E. P. Dowker and R. I. Smith, Rietveld structure refinement of precipitated carbonate apatite using neutron diffraction data, *Biomaterials*, 2004, **25**, 2205–2213.
34 R. Z. Legeros, O. R. Trautz, J. P. Legeros, E. Klein and W. P. Shirra, Apatite Crystallites: Effects of Carbonate on Morphology, *Science*, 1967, **155**, 1409–1411.
35 S. Kannan, J. M. G. Ventura, A. F. Lemos, A. Barba and J. M. F. Ferreira, Effect of sodium addition on the preparation of hydroxyapatites and biphasic ceramics, *Ceram. Int.*, 2008, **34**, 7–13.
36 I. R. Gibson, I. Rehman, S. M. Best and W. Bonfield, Characterization of the transformation from calcium-defcient apatite to β-tricalcium phosphate, *J. Mater. Sci.: Mater. Med.*, 2000, **12**, 799–804.
37 A. Yasukawa, K. Kandori and T. Ishikawa, TPD-TG-MS Study of Carbonate Calcium Hydroxyapatite Particles, *Calcif. Tissue Int.*, 2003, **72**, 243–250.
38 N. Elazarifi, A. Ezzamarty, J. Leglise, L. C. de Ménorval and C. Moreau, Kinetic study of the condensation of benzaldehyde with ethylcyanoacetate in the presence of Al-enriched fluoroapatites and hydroxyapatites as catalysts, *Appl. Catal., A*, 2004, **267**, 235.
39 S. Kannan, I. A. F. Lemos, J. H. G. Rocha and J. M. F. Ferreira, Synthesis and characterization of magnesium substituted biphasic mixtures of controlled hydroxyapatite/β-tricalcium phosphate ratios, *J. Solid State Chem.*, 2005, **178**, 3190–3196.
40 M. E. Fleet and X. Liu, Coupled substitution of type A and B carbonate in sodium-bearing apatite, *Biomaterials*, 2007, **28**, 916–926.
41 G. Bonel, Contribution a l'etude de la carbonatation des apatites. I. Synthese et etude des proprietes physico-chimiques des apatitescarbonatees du type A, *Ann. Chim.*, 1972, **7**, 65–88.
42 J. C. Elliott, Space group and lattice constants of $Ca_{10}(PO_4)_6CO_3$, *J. Appl. Crystallogr.*, 1980, **13**, 618–621.
43 A. Krajewski, M. Mazzochi, P. L. Buldini, A. Ravaglioli, A. Tinti, P. Taddei and C. Fagnano, *J. Mol. Struct.*, 2005, **744**, 221–228.
44 Z. R. Hinedi, S. Goldberg, A. C. Chang and J. P. Yesinowski, A ^{31}P and ^{1}H MAS NMR study of phosphate sorption onto Calcium carbonate, *J. Colloid Interface Sci.*, 1992, **152**, 141–160.
45 C. Jager, T. Welzel, W. Meyer-Zaika and M. Epple, A solid-state NMR investigation of the structure of nanocrystalline hydroxyapatite, *Magn. Reson. Chem.*, 2006, **44**, 573–580.
46 S. Sugiyama, T. Miyamoto, H. Hayashi and J. B. Moffat, Effects of non-stoichiometry of calcium and strontium hydroxyapatites on the oxidation of ethane in the presence of tetrachloromethane, *J. Mol. Catal. A: Chem.*, 1998, **135**, 199–208.
47 N. S. Resende, M. Nele and V. M. M. Salim, Effect of anion substitution on the acid properties of hydroxyapatite, *Thermochim. Acta*, 2006, **451**, 16–21.

48 T. Kawasaki, S. Takahashi and K. Ikeda, Hydroxyapatite high-performance liquid chromatography: column performance for proteins, *Eur. J. Biochem.*, 1985, **152**, 361–371.

49 S. Ogo, A. Onda, Y. Iwasa, K. Hara, A. Fukuoka and K. Yanagisawa, 1-Butanol synthesis from ethanol over strontium phosphate hydroxyapatite catalysts with various Sr/P ratios, *J. Catal.*, 2012, **296**, 24–30.

50 A. Gervasini, C. Messi, D. Flahaut and C. Guimon, Acid properties of iron oxide catalysts dispersed on silica-zirconia supports with different Zr content, *Appl. Catal., A*, 2009, **367**, 113–121.

51 L. Silvester, J.-F. Lamonier, J. Faye, M. Capron, R.-N. Vannier, C. Lamonier, J.-L. Dubois, J.-L. Couturier, C. Calais and F. Dumeignil, *Green Chem.*, 2014, to be submitted.